



Cloud liquid water path at the North Slope of Alaska is largely insensitive to local meteorology in Arctic winter

Kara Hartig^{1,2}, John J. Cassano^{1,2,3}, Matthew D. Shupe^{1,2,4}, and Amy Solomon^{1,2,4}

¹Cooperative Institute for Research in Environmental Sciences, Boulder, CO

²National Snow and Ice Data Center, Boulder, CO

³Atmospheric and Oceanic Sciences Department, University of Colorado-Boulder, Boulder, CO

⁴NOAA Physical Sciences Laboratory, Boulder, CO

Correspondence: Kara Hartig (kara.hartig@colorado.edu)

Abstract. Mixed-phase clouds in the Arctic are tightly coupled to the surface energy budget in the cold months, helping to set surface temperatures and sea ice extent. However, the meteorological conditions that give rise to these clouds and their remarkable persistence across the Arctic are not well constrained, leading to model biases. Using over a decade of observations from the North Slope of Alaska, this research investigates the relationships between cloud base temperature and moisture, bulk atmospheric moisture, wind direction, large-scale circulation, and cloud liquid and ice water path. Liquid-containing clouds are ubiquitous at this site, occurring 60-70% of the time between November and March, although about half of those cases have a liquid water path under 10 g m^{-2} . We find that liquid water path is remarkably insensitive to temperature, moisture, wind direction, and large-scale circulation. Furthermore, meteorological regimes with significant differences in temperature, moisture, and cloud fraction do not produce appreciable differences in cloud liquid water path. Ice water path, on the other hand, is correlated with bulk atmospheric moisture, with particularly strong increases when precipitable water vapor exceeds the 90th percentile, and may be responsible for the muted response of liquid water path to high atmospheric moisture. To explain the observed sensitivity of ice water path and insensitivity of liquid water path to meteorology and large-scale circulation, we propose a series of hypotheses centered around continuous radiative cooling in a stable environment and the role of ice in enabling or limiting liquid mass accumulation.

1 Introduction

Clouds play a crucial role in Arctic climate. For most of the year, their longwave radiative surface warming effect outweighs their shortwave radiative cooling effect, leading to surface warming (Walsh and Chapman, 1998; Shupe and Intrieri, 2004; Stramler et al., 2011; Graham et al., 2017). These impacts are largely driven by liquid-containing or mixed-phase clouds, which have the strongest interaction with atmospheric radiation. Liquid-containing clouds are ubiquitous in the Arctic, occurring 20-50% of the time even in winter over a wide range of environs (Mioche et al., 2015; Cesana et al., 2012; Shupe et al., 2006, 2011), making them a significant influence on surface conditions. Clouds influence the atmosphere itself as well, helping to cool and dry air masses that pass through polar regions (Ali and Pithan, 2020; Pithan et al., 2018). However, the Arctic is challenging and expensive to monitor, contributing to limited observations that nonetheless reveal large and persistent model biases across

a wide range of environments, seasons, and meteorological conditions (Davy and Outten, 2020; Cai et al., 2021). Uncertainties
25 around cloud processes and model representations have been identified as a major source of Arctic model biases (Medeiros
et al., 2011; Pithan and Mauritsen, 2014; Solomon et al., 2023), leaving clouds a prime target for further study.

Arctic clouds form, persist, and eventually dissipate as part of a continuous process of air mass transformation. In polar
regions, clouds are believed to play a particularly active role in the transformation of warm, moist mid-latitude air into cold,
dry polar air (Cronin and Tziperman, 2015; Pithan et al., 2018; You et al., 2022). When a relatively warm, moist air mass is
30 advected over a colder surface like polar sea ice or land, the near-surface air begins to cool, eventually reaching saturation
to form clouds. Cloud liquid produces intense radiative cooling at cloud top while radiatively warming the surface to drive
buoyant mixing, redistributing their radiative cooling and triggering a host of interacting processes (Morrison et al., 2012).
Importantly, the liquid layers in these clouds are often the source of ice particle initiation, followed by rapid ice growth. Cloud
ice is ultimately responsible for dissipating the cloud by precipitating out its moisture, although this can be a slow process due
35 to weak precipitation and humidity inversions at cloud top that resupply fresh moisture through entrainment (Curry et al., 1988;
Sedlar and Tjernström, 2009; Solomon et al., 2011). The air mass transformation framework suggests a kind of characteristic
Arctic cloud lifecycle where warmer, moister air masses form clouds that eventually glaciate and leave behind colder, drier
polar air, but observational evidence is limited and leaves many questions concerning how such transformations shape Arctic
cloud occurrence.

Liquid-containing Arctic clouds can have lasting impacts on underlying surfaces. The presence or absence of liquid-containing
40 clouds is one of the main distinguishing factors between the two states of the characteristic bimodal surface energy distribution
that has been identified at many ground-based observatories across the Arctic (Stramler et al., 2011; Cox et al., 2012; Graham
et al., 2017; Silber and Shupe, 2022; Solomon et al., 2023; Shupe et al., 2026) as well as in satellite observations (Cesana
et al., 2012; Bertossa and L'Ecuyer, 2024). By reducing energy lost from the surface, liquid-containing clouds increase surface
45 temperature relative to clear sky conditions (Stramler et al., 2011; Graham et al., 2017). These impacts on temperature and
downwelling radiation can lead to persistent changes in sea ice concentration and snow pack by altering the surface energy
budget by tens of W/m^2 in crucial growth or melt periods (Zhang et al., 1996; Francis and Hunter, 2006; Maksimovich and
Vihma, 2012; Philipp et al., 2020; Shupe et al., 2026). In an air mass transformation context, atmospheric rivers that inject
heat and moisture from lower latitudes into the Arctic have been found to increase cloud fraction, cloud liquid, and cloud ice
50 content, increase surface temperature by around $10^{\circ}C$, and reduce sea ice concentration (You et al., 2022; Liu et al., 2018;
Doyle et al., 2011; Woods et al., 2013; Pithan et al., 2018; Kirbus et al., 2023; Woods and Caballero, 2016). However, moisture
intrusions represent an extreme perturbation, and it is unclear whether the relationship between atmospheric temperature and
moisture and cloud properties also holds for more typical conditions.

In mixed-phase clouds containing both liquid and ice, the distribution of condensed mass into liquid and ice is complicated
55 by interactions between the two. Between -38 and $0^{\circ}C$, supercooled liquid droplets generally need to encounter ice nucleating
particles (INPs) to initiate freezing (DeMott et al., 2010; De Boer et al., 2011), making liquid droplets nearly a prerequisite for
forming ice. However, when ice and supercooled liquid coexist in the same volume, the difference in saturation vapor pressure
between the two causes vapor to preferentially deposit on ice and evaporate from liquid, which can rapidly transfer mass from



liquid to ice phase in the Wegener-Bergeron-Findeisen (WBF) process (Wegener, 1911; Bergeron, 1935; Findeisen, 1938).
60 The effect of ice on liquid is particularly apparent in the seeder-feeder mechanism, in which ice crystals precipitating into a
liquid-containing cloud layer tend to thin or even disperse that layer (Shupe et al., 2013; Korolev et al., 2017; Achtert et al.,
2026) through the WBF mechanism and/or riming. How Arctic mixed-phase clouds regularly persist for hours and even days
in spite of the WBF process is an enduring puzzle in Arctic cloud research (Morrison et al., 2012; Shupe, 2011; Zuidema et al.,
2005; Verlinde et al., 2007). The WBF process, along with a host of other mechanisms including secondary ice production and
65 riming (Field et al., 2017; Korolev and Leisner, 2020), serves to highlight the challenge of connecting the microscale to the
macroscale and identifying the conditions that are favorable for cloud liquid versus cloud ice.

This study was designed to explore the influence of temperature, moisture, wind direction, and large-scale circulation on
wintertime cloud phase with a particular focus on liquid water path using long-term measurements from the North Slope of
Alaska. Since a moist adiabat ties condensed mass to cloud base conditions, we expected a strong relationship between liquid
70 water path, cloud base temperature, and cloud depth. Given the response of cloud liquid to moisture intrusions, we anticipated
a response to bulk atmospheric moisture as well. Additionally, an air parcel transformation framework suggests that air mass
history, approximated by the circulation, may modify the liquid water path: whether a cloud layer is forming or dissipating,
or how developed the ice production has become, for example. Instead, the observations presented here reveal a remarkable
insensitivity of liquid water path to meteorological controls. In this paper, we explore the relationships outlined above to
75 develop hypotheses explaining the remarkable resilience of liquid-containing clouds in the Arctic.

2 Data & Methods

The primary data sources for this study are all taken from the North Slope of Alaska (NSA), a U.S. Department of Energy
Atmospheric Radiation Measurement (ARM) User Facility (Verlinde et al., 2016). To maximize overlap between the different
instruments while avoiding systematic biases from changes to specific instruments, the period from 12 November 2011 through
80 31 December 2023 is used for all ARM NSA data. An extended winter season is defined for this analysis, running from the start
of November when the annual cycle of cloud fraction begins to decline to the end of March when it increases again each year
Shupe et al. (2011), and all data is restricted to this seasonal window. A summary of the instruments and their corresponding
measurements used in this study is provided in Table 1 and described in detail below.

Soundings are a backbone of this analysis. Radiosondes are released up to 4 times per day from NSA, and the resulting
85 soundings are subject to quality checks run by ARM NSA on the Vaisala-processed temperature, humidity, wind direction, and
wind speed to produce vertical profiles. For this analysis, these profiles are linearly interpolated onto a shared height coordinate
from 8 to 12,000 meters in 5-meter increments and each sounding is assigned a timestamp corresponding to the launch time
of the radiosonde. Using extended winter data from 2011 through 2023 results in 4,791 valid soundings after dropping the
handful that did not report data up to at least 1,000 m.

90 Saturated layers, a proxy for regions containing cloud liquid water, are derived from soundings after the hourly averaging
process described later in this section by first looking for regions where relative humidity with respect to liquid water is



Table 1. Instrument & Dataset Details from North Slope of Alaska (ARM NSA). Datastream names are as they appear in the ARM data repository.

Instrument	Variables	Datastream	Native Resolution	Derived Variables
Sounding	T, q, RH, u, v, w	nsasondownpnC1.b1	time: 0-4 per day, vertical: 5-8 m	saturated layers
Cloud Radar	reflectivity	nsakazrcorgeC1.c1 (2011-2014), nsakazrcorgeC1.c0 (2014-2019), nsakazrcfrorgeC1.c0 (2019-2023)	time: 4-5 seconds, vertical: 30 m	cloud fraction, IWP, clear sky flag
Microwave Radiometer	LWP, PWV	nsamwrret1iljclouC1.c2	time: 20-30 seconds	–
Ceilometer	first cloud base height	nsaceilC1.b1	time: 15 seconds	–

greater than 95%. One could use a restrictive threshold of 100% or more to identify liquid-saturated regions, but there is a combined uncertainty of 3% reported for relative humidity measurements for the instrument used at NSA (Keeler, 2025), potentially leaving out many saturated cases. Furthermore, a simple inspection of sonde profiles across multiple variables and comparison to other instruments like the cloud radar and microwave radiometer quickly reveals many cases that almost certainly have liquid-containing clouds even where the measured relative humidity is a few percent below 100%. Except where explicitly stated otherwise, a threshold of 95% relative humidity for saturated layers will be used throughout this study, which is consistent with previous studies at NSA validated against lidar measurements (Silber et al., 2020, 2021) and is between the mean and median relative humidity at the first cloud base height reported by the ceilometer (Fig. A1a). To reduce the ability of small relative humidity fluctuations about the threshold to break up cloud layers, any below-threshold gap of 30 m or less with saturated layers above and below is filled in to create a continuous saturated layer. Conversely, any saturated region less than 30 m deep is not considered a saturated layer. From these saturated layers, we determine the total saturated depth (sum of all saturated layer depths in a profile), the number of individual saturated layers, and the height of each layer base and top.

A 35-GHz Ka-band zenith-pointing Doppler cloud radar provides vertical profile measurements of reflectivity in 30-meter bins at a temporal resolution of about 5 seconds. This study uses the general mode, which is less sensitive to high clouds but captures lower regions expected to include most liquid-containing clouds. We interpolate all reflectivities onto a shared height coordinate from 105 to 12,000 meters in 30-meter increments and exclude reflectivity values with signal-to-noise ratio less than -13 dB. The vertically-resolved cloud fraction is approximated by vertical profiles of radar reflectivity, which is sensitive to any hydrometeors and therefore includes both clouds and precipitation. Two quantities are derived from these reflectivity profiles, ice water path and a clear sky flag, both of which are calculated after the hourly averaging described later in this section. The ice water path is calculated from the vertical integral of the ice water content $IWC = aZ_e^b$, which depends on the



radar reflectivity Z_e and two constants $a = 0.1$ and $b = 0.63$, where a is chosen to match the winter average for that parameter determined at the nearby SHEBA site (Shupe et al., 2005) and b is the average suggested by (Matrosov, 1999). We define clear sky to be times when at least 99% of the bins in the vertical have no detected reflectivity (i.e. no reflectivity values above the signal-to-noise ratio) up to 10 km and there are no continuous regions of detected reflectivity deeper than 100 meters.

A microwave radiometer provides best-estimate values for liquid water path (LWP) and precipitable water vapor (PWV) based on measurements of downwelling radiation at 23.8 and 31.4 GHz. The product used here is a value-added product provided by ARM that employs a physical retrieval method and clear-sky brightness temperature offsets to capture the conditions at NSA (Turner et al., 2007). The reported theoretical uncertainty for LWP is around 25 g m^{-2} (Turner et al., 2007; Westwater et al., 2001), but in practice the uncertainty is smaller. The 25 g m^{-2} value corresponds to the maximum LWP retrieved during clear-sky conditions and conceals the fact that the vast majority of clear-sky measurements are within a few g m^{-2} of the expected zero (Fig. A1c). Comparison to radiosondes indicates 97% of LWP retrievals in winter at NSA above 10 g m^{-2} and 65% between 0 and 10 g m^{-2} have identified saturated layers overhead (see Fig. 1 and accompanying discussion below). In practice, bulk statistics exhibit no retrieval bias (Cadeddu et al., 2009, 2013) and LWP retrievals have much smaller errors. To accommodate the high-uncertainty/low-bias of LWP retrievals, this study always uses either the full LWP distribution and its descriptive statistics or, when splitting LWP into categories, separates out values below 10 g m^{-2} to account for the spread in LWP during clear sky conditions (Fig. A1c) and the decrease in cases with a corresponding saturated layer detected by the sounding (Fig. 1).

Ceilometer measurements of the lowest cloud base height from the standard, proprietary detection produced by Vaisala at 10-m resolution are provided by a Vaisala Laser Ceilometer, Model CL31.

Given the need throughout the analysis to consider vertically-resolved meteorological and cloud properties, all ARM NSA data presented here and described above is coordinated with the soundings. For each radiosonde launch time, data from the cloud radar, microwave radiometer, and ceilometer are averaged over the following hour to provide measurements corresponding to that sounding. Missing data is ignored in the hourly average, and for the cloud radar reflectivity at least half of the times used to calculate the hourly average must have reflectivity measurements to be preserved in the average. This procedure generates a library of multi-instrument measurements and derived quantities at NSA across 4,791 timestamps for use in this study, spanning the extended winter season from the end of 2011 to the end of 2023. Of these 4,791 cases, data is missing for <1% of radar profiles, 22% of microwave radiometer measurements, and 4% of ceilometer measurements.

The adiabatic liquid water path $LWP_{adiabatic}$ is used to determine how well observations of LWP match the amount of condensed liquid water expected for a well-mixed cloud given the cloud base temperature and pressure and total cloud depth:

$$LWP_{adiabatic} = \int_{z_0}^{z_{top}} LWC_{adiabatic} dz \quad (1)$$

where z_0 is the base of the liquid cloud layer, z_{top} is the top, and $LWC_{adiabatic}$ is the adiabatic liquid water content in g m^{-3} and defined as follows based on Eytan et al. (2021):



$$LWC_{adiabatic} \approx \int_{z_0}^{z_{top}} \frac{A_1(z)}{A_2(z)} dz \quad (2)$$

$$A_1(z) = \frac{g}{T} \left(\frac{L_w}{c_p R_v T} - \frac{1}{R_a} \right) \quad (3)$$

$$A_2(z) = \frac{1}{\rho_v} + \frac{L_w^2}{c_p R_v T^2 \rho_d} \quad (4)$$

where g is gravitational acceleration, T is temperature, L_w is latent heat of water evaporation, c_p is specific heat of air at constant pressure, R_v is specific gas constant of water vapor, R_a is specific gas constant of air, ρ_v is density of water vapor, and ρ_d is density of dry air. We take A_1/A_2 to be constant over the cloud layer, a common assumption leading to a linear $LWC_{adiabatic}$ profile (Eytan et al., 2021), by using T and pressure (for calculating ρ) at cloud base.

Regional context for the large-scale circulation is provided by a self-organizing maps (SOM) analysis, which uses an unsupervised neural network to group data by shared spatial patterns into a specified number of dominant patterns called nodes (Kohonen, 1990; Hewitson and Crane, 2002; Cassano et al., 2015). Hourly sea level pressure (SLP) from the ERA5 reanalysis (Hersbach et al., 2020; C3S, 2018) at 0.25 degree resolution in latitude and longitude from January 2000 to December 2024 is used to characterize the large-scale circulation. The data is first pulled at 6-hour intervals for the extended winter season from November through March. Sea level pressure fields are then interpolated onto the EASEv2 25-km grid (Brodzik et al., 2012), which gives equal areas equal weights in the SOM analysis, and reduced to an EASE-defined domain centered on NSA spanning $i = (100, 230)$ and $j = (150, 280)$. Land points with a surface elevation greater than 500 meters above sea level are masked out to avoid extended interpolations of pressure down to sea level. Finally, anomalies are calculated at each time step by removing the average over the remaining domain from the sea level pressure value at each point. The use of SLP anomalies to train the SOM is consistent with previous studies using SOMs (Cassano et al., 2006, 2015; Gallagher et al., 2018; Hewitson and Crane, 2002) and preserves the spatial gradients in the SLP field, which drive the atmospheric circulation, while removing day-to-day variability in the magnitude of SLP. Training of an optimal SOM for identifying circulation patterns impacting the NSA follows the approach described in Cassano et al. (2015). The resulting sea level pressure anomalies are then used to train SOMs in a 3x2, 4x3, and 5x4 node configuration, using all combinations of the hyperparameters $\alpha = (0.005, 0.01, 0.02, 0.03, 0.04, 0.05)$, $r_{len} = (1000, 5000, 10000, 25000, 50000, 100000)$, and r the integers from 1 to N where N is the total number of nodes for that configuration. The resulting SOMs are then ranked within each configuration according to their quantization error, which is proportional to the sum of the squared differences between the input data and the nodes to which they map. The top 10 are inspected to discard any with twisted Sammon maps, a visualization method portraying the Euclidean distances between each SOM node and its neighbors which is described in Cassano et al. (2015), and to check for major variations. A final SOM is selected for each configuration from the remaining options such that the node layout is largely consistent across the three configurations. For this analysis, we determined the 4x3 SOM to be most appropriate, as it was the smallest that resulted in sea level pressure anomalies capturing all major wind direction regimes observed at NSA. The original sea level pressure anomalies every 6 hours are then related back to the SOM nodes, where each timestamp is assigned its closest matching node



175 pattern, identified as having the smallest squared difference between the node SLP anomalies and the individual timestamp SLP anomalies. Composites of NSA data are constructed for each node by finding the closest node pattern to each sounding launch time (excluding soundings more than 2 hours from the nearest 6-hourly timestamp, 2% of all sounding times) and averaging over all NSA data assigned to that node.

3 Results

180 3.1 Liquid-containing cloud occurrence by instrument

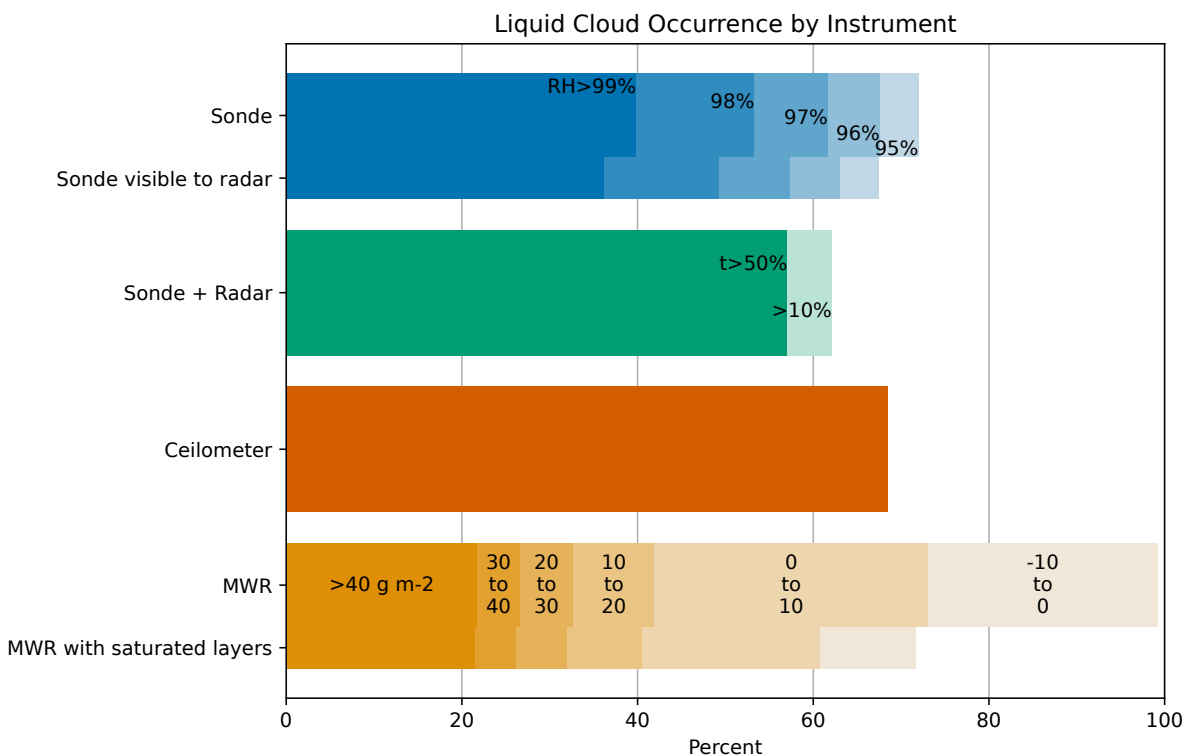


Figure 1. Liquid-containing clouds are ubiquitous at the North Slope of Alaska in winter, but the precise liquid cloud fraction varies by instrument and detection threshold. Each bar shows the percent of the time that liquid-containing clouds were detected by the corresponding instrument for November through March of 2011-2023. All percents are relative to times when no instruments (sonde, radar, ceilometer, and MWR) were missing data, for a total of 3,400 data points. Shading for the ‘Sonde’ bars corresponds to different relative humidity thresholds from 95% (pale blue) to 99% (dark blue), while ‘Sonde in radar range’ shows the same but only based on sonde readings above 165 m, which is the lowest range gate detected by the cloud radar. ‘Sonde + Radar’ is based on times when the relative humidity was above 95% and the cloud radar detected hydrometeors in at least one of the liquid-saturated regions. Over 50% of values at a given height had to be above the signal-to-noise threshold to be retained in the hourly average for $t > 50\%$, and only 10% for $t > 10\%$. ‘Ceilometer’ is based on times when the ceilometer detected at least one cloud base height. ‘MWR’ is shaded according to the liquid water path in g m^{-2} , displayed in bins from highest (dark gold) to lowest (pale gold) values, while ‘MWR with saturated layers’ shows the same liquid water path bins but only for times when at least one saturated layer was detected in the corresponding sonde.



Given this study's focus on liquid-containing clouds, it is sensible to consider how liquid cloud fraction varies by measurement method across the suite of instruments deployed at the NSA site. Figure 1 shows the liquid-containing cloud occurrence between November and March from 2011 through 2023 according to radiosondes, cloud radar, ceilometer, and microwave radiometer. Broadly speaking, the liquid-containing cloud occurrence in winter hovers around 60% but, depending on the instrument in question and the threshold used to define a positive detection, can vary anywhere from 40 to 75%.

Each instrument illustrates the challenge of identifying cloud liquid in a different way. For "Sonde", there is fundamental measurement uncertainty in the relative humidity; the instrument used at NSA has a reported combined uncertainty of 3% for relative humidity measurements (Keeler, 2025) and comparison of individual cases to the other instruments presented in Fig. 1 reveal many liquid-containing cloud layers even when relative humidity is below 100%. Throughout the rest of this study, a threshold of 95% will be used, which is consistent with previous studies at NSA (Silber et al., 2020, 2021). Since the cloud radar's lowest range gate is at 165 m, the "Sonde visible to radar" bar is based strictly on relative humidity at and above this height. The difference between "Sonde" and "Sonde visible to radar" indicates that about 3% of the time the only liquid-containing clouds present are in the bottom 165 m of the atmosphere. These detections may be fogs or other very low level clouds with limited vertical extent. "Sonde + Radar" requires both a relative humidity above 95% and detected radar reflectivity in the same height bin at the same time; the difference between this class and "Sonde" represents cases when the cloud radar did not detect hydrometeors at the same height that the soundings identified liquid-saturated cloud layers. Part of the challenge in comparing sonde to radar is in imperfect co-location; the cloud radar, ceilometer, and microwave radiometer are all at a fixed ground-based site, although with different fields of view, while the radiosonde both drifts from its release point and samples only its immediate vicinity, increasing the probability of disagreement with other instruments in a spatially heterogeneous cloud field. "Ceilometer" detects a cloud base at frequencies in line with both radiosondes and the microwave radiometer. However, the median first cloud base height derived from the ceilometer is 477 m higher than that derived from radiosondes (Fig. A1b), so the two instruments are not necessarily detecting the same liquid-containing cloud layers at a given time. Since the ceilometer is an optical instrument, optically thick ice clouds are likely to contaminate some of the ceilometer cloud base height detections, contributing to this study's reliance on other instruments for liquid-containing cloud detection throughout the rest of this analysis. Finally, the microwave radiometer "MWR" reports a best-estimate liquid water path that is displayed in bins of 10 g m^{-2} from -10 up to 40 plus one bin for all values higher than that. Setting any particular threshold to identify a true positive liquid water path is tricky; we estimate the effective uncertainty to be around 10 g m^{-2} , but comparison to saturated layers identified by the radiosondes ("MWR with saturated layers") indicates that most of the measurements in the $0 - 10 \text{ g m}^{-2}$ range correspond to identifiable cloud liquid. Liquid water path features heavily in this study, as it is one of the main determining factors of the surface radiative impact of clouds, so the analysis that follows will use a combination of broad liquid water path bins and correspondence with positive detections by other instruments to select for significant liquid water path values.

Whichever instrument or detection threshold is used, it is clear from Fig. 1 that liquid-containing clouds are extremely common at the North Slope of Alaska in winter. However, the longwave radiative impact of those clouds can vary widely depending on their opacity (closely related to the liquid water path) and temperature. Downwelling longwave radiation from



liquid-containing clouds in Arctic winter increases dramatically with liquid water path up to about 30 or 40 g m^{-2} (Fig. A2). Beyond that, the cloud emissivity approaches unity, i.e. the cloud becomes opaque, such that increasing cloud liquid does not further increase the downwelling longwave irradiance. Liquid water paths below about 40 g m^{-2} are therefore of particular interest, as they represent the range within which relatively small variations in liquid water path or other cloud properties produce large changes in surface radiative impact. Two questions naturally arise: what conditions are favorable for liquid-containing clouds, and what factors control how much liquid those clouds have?

3.2 Cloud base controls on LWP

Previous work has shown liquid water path in the Arctic to depend on cloud base temperature, albeit in summer (Lin et al., 2003) or in idealized models (Zhang et al., 2020). The adiabatic liquid water path framework also predicts dependence on cloud base temperature, so we next investigate this relationship. Given the longwave radiative dependencies just discussed, we focus on three categories of liquid water path: Thin cases, where LWP is less than 10 g m^{-2} and therefore within the effective uncertainty range of zero for the radiometer; Semi-transparent cases, where LWP is between 10 and 40 g m^{-2} and the surface radiative effect is particularly sensitive to changes in liquid content; and Opaque cases, where LWP is above 40 g m^{-2} and the longwave radiative effect of the cloud is saturated.

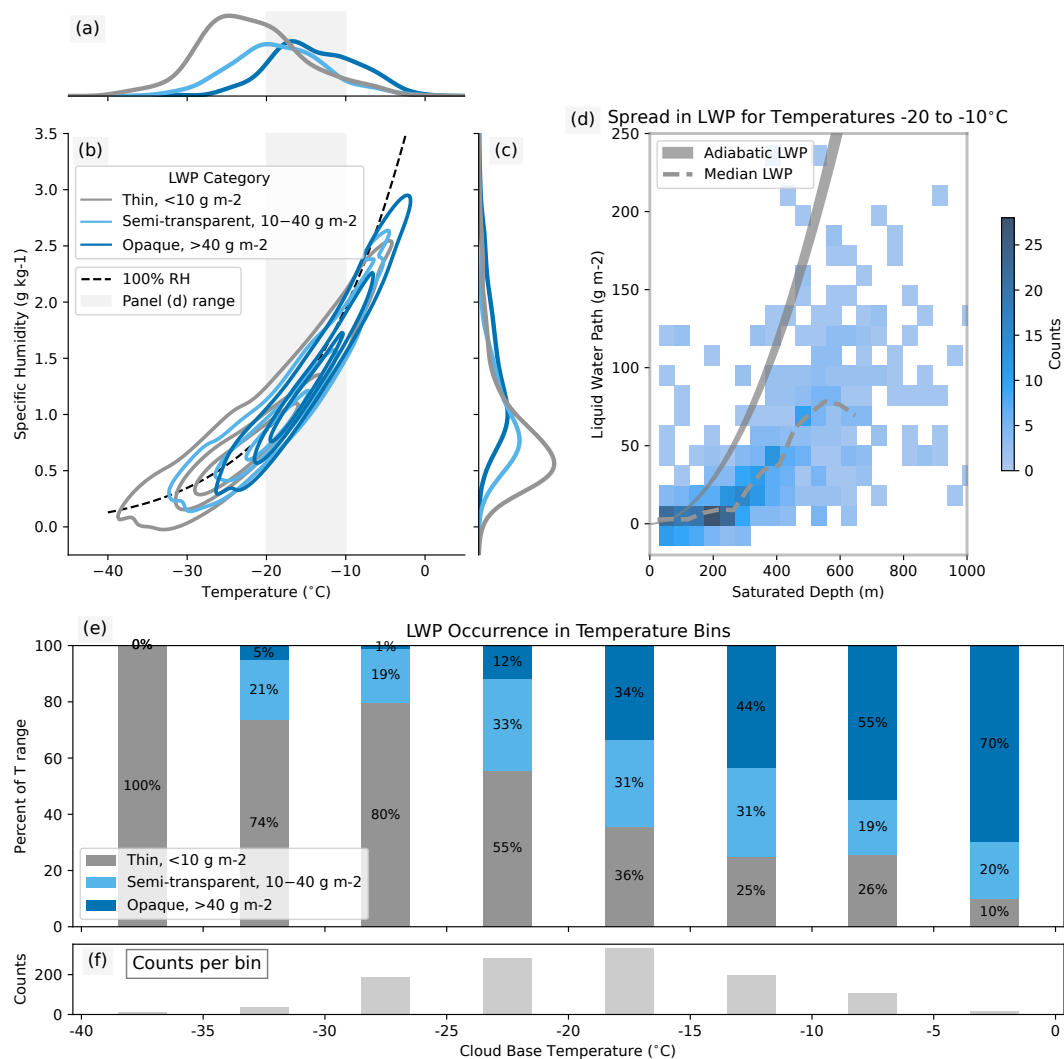


Figure 2. The highest and lowest wintertime cloud base temperatures have distinct liquid water paths, but the three liquid water path categories occur at similar frequencies throughout the middle, and most common, part of the supercooled temperature range. In the upper left, the middle plot (b) is a joint PDF of cloud base temperature versus cloud base specific humidity at times with only one liquid-saturated cloud layer. Contours are drawn at 0.1, 0.4, and 0.7 iso-proportions of density, i.e. 0.1 means 10% of the probability mass lies outside that contour, for three different liquid water path ranges separated at 10 and 40 g m⁻². The dashed line corresponds to a relative humidity of 100%. The border plots are marginal distributions for temperature (a) and for specific humidity (c) as kernel density plots. The grey shaded box in (b) highlights the temperature range shown in (d), which compares liquid water path to saturated depth between -20 and -10°C. The grey shaded curve corresponds to the predicted adiabatic liquid water path (Eq. 1) as a function of saturated depth spanning the same temperature range and using the median pressure at saturated layer base. Panel (e) shows the same data as (a) but with each LWP category as a percentage of the cloud base temperature bin, with the total number of cases per bin in (f).



230 The relationship between cloud base temperature, specific humidity, and liquid water path is shown in Fig. 2. Since the
cloud base conditions are tied to a single cloud layer whereas liquid water path is a column-aggregated measurement, data in
the figure is restricted specifically to cases with only one liquid-saturated layer as identified by the sounding. While cases were
not selected for any particular temperature, it happens that nearly all single-layer cloud bases in the months and years analyzed
fall in the supercooled liquid temperature range between about -38 and 0°C . Each observation shown has both a defined liquid
235 water path from the microwave radiometer and a saturated layer detection from the sounding, so at least two instruments agree
that liquid water is present.

As they must, observations of cloud base conditions in panel (b) lie close to the black dashed Clausius-Clapeyron relationship
between temperature and specific humidity at 100% saturation, indicating that either variable could reasonably be used to
describe the cloud base state. In the broadest sense, liquid water path is a function of cloud base temperature. Panel (e),
240 showing the breakdown into LWP categories by cloud base temperature, demonstrates that the coldest cases below -25°C have
under 10 g m^{-2} of liquid water more than two-thirds of the time, while the warmest cases above -5°C are almost always opaque.
However, at intermediate temperatures between -25 and -5°C , any of the three liquid water path categories is possible. To be
specific, 73% of all observations occur at temperatures with over a 10% occurrence of all three liquid water path categories. The
semi-transparent case, with liquid water paths between 10 and 40 g m^{-2} , is particularly insensitive to temperature, occurring
245 in roughly 20 to 30% of cases at every temperature between -35 and 0°C . Rather than shift with temperature, the liquid water
path distribution changes shape, preserving both very low and very high values at almost all temperatures in the supercooled
liquid range.

To determine whether cloud depth can explain the variation in liquid water path at a given cloud base temperature, Fig. 2d
shows the relationship between liquid water path and saturated depth for cloud base temperatures between -20 and -10°C ,
250 highlighted with a grey box in panel (b). Liquid water path scales with saturated depth reasonably well, but the spread is large,
particularly in the semi-transparent regime, with saturated depths from 200 to nearly 800 m producing the same liquid water
path. Liquid water path is also significantly sub-adiabatic under these conditions, with values falling well below the shaded
region indicating the predicted liquid water path for a given cloud base temperature and saturated depth. While the co-existence
of ice can produce a sub-adiabatic liquid water path, the amount of cloud ice within the liquid-containing layer does not fully
255 explain the departure from adiabaticity for these clouds (Fig. A3).

3.3 Meteorological controls on LWP

Instantaneous cloud base conditions and total cloud depth are clearly not enough to explain liquid water path alone. But clouds
do not develop in isolation. Moisture, shear, inversions, turbulence, and more in the surrounding environment can interact with
cloud layers and influence their properties. Atmospheric rivers have been shown to increase cloud water and cloud liquid (Liu
260 et al., 2018; You et al., 2022), so perhaps it is the bulk moisture and temperature of the air mass rather than the conditions
just at cloud level that shape the liquid water path. The covariance between precipitable water vapor (PWV), which is the total
amount of water vapor in a vertical column, and cloud liquid and ice is considered next.

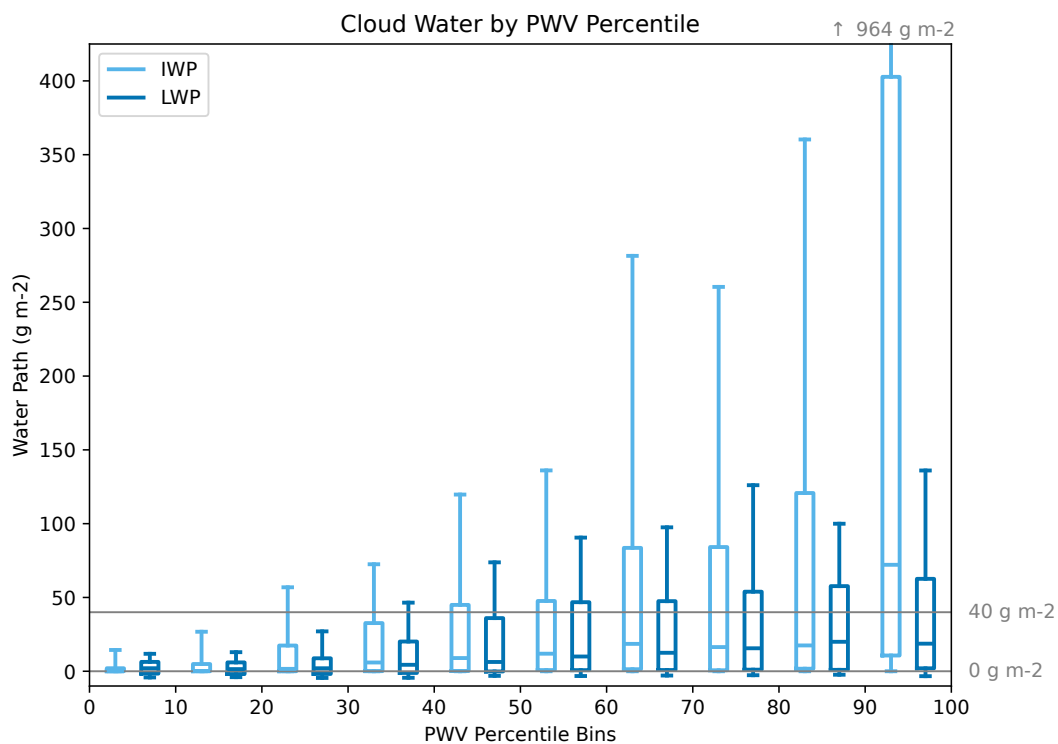


Figure 3. Both ice and liquid water path are sensitive to bulk moisture, but liquid less so. Box-and-whisker plots for ice (light blue) and liquid (dark blue) water path as a function of precipitable water vapor (PWV) percentile range are shown, where PWV is the microwave radiometer best estimate. Whiskers extend to the 10th and 90th percentiles of cloud water path. Grey horizontal lines bracketing the semi-transparent regime for liquid at 0 and 40 g m⁻² are included for reference, as well as the above-axis whisker height for ice water path in the 90-100 percentile range.



Figure 3 shows the liquid and ice water paths as a function of precipitable water vapor percentile, utilizing the full data set rather than just single-layer liquid cases. It is immediately apparent that both cloud liquid and cloud ice increase with PWV. The largest difference is in the occurrence of high cloud water values, with the 75th percentile (top of each box) increasing from 2 to 403 g m⁻² for ice and 6 to 63 g m⁻² for liquid between the lowest and highest PWV bins. Ice is more sensitive in the middle of the distribution as well, with the median ice water path increasing from 0 to 72 g m⁻² over the same range while liquid water path goes from 2 to just 19 g m⁻². However, the increase in liquid water path stagnates in the highest PWV bins. While ice water path increases dramatically in the 90th percentile of PWV, none of the liquid water path distributions above the 60th percentile are significantly different from each other (Fig. A4) at the 95% level using a Kolmogorov-Smirnov test (hereafter the standard for “significantly different”). A muted response of liquid water path to high atmospheric water vapor has also been observed at Summit, Greenland (Wedum et al., 2026). The differing responses of liquid and ice at the highest PWV values indicates that most of the excess available moisture is going into ice rather than liquid. But even as the high end of cloud water increases with PWV, the low end persists. Over half of all cloud scenes above the 90th percentile of PWV have less than 50 g m⁻² of total condensed water (Fig. A5). Conversely, radiatively opaque liquid-containing clouds appear at least 10% of the time by the 30th percentile bin of PWV, so they clearly do not require particularly moist conditions to form.

Temperature and moisture certainly play some role in setting liquid water path. But it is equally true that virtually any commonly occurring temperature or moisture, be it at cloud level or for the air mass as a whole, can support virtually any liquid water path. Next, we extend to information about wind direction as a proxy for air mass age and coupled temperature-moisture conditions.

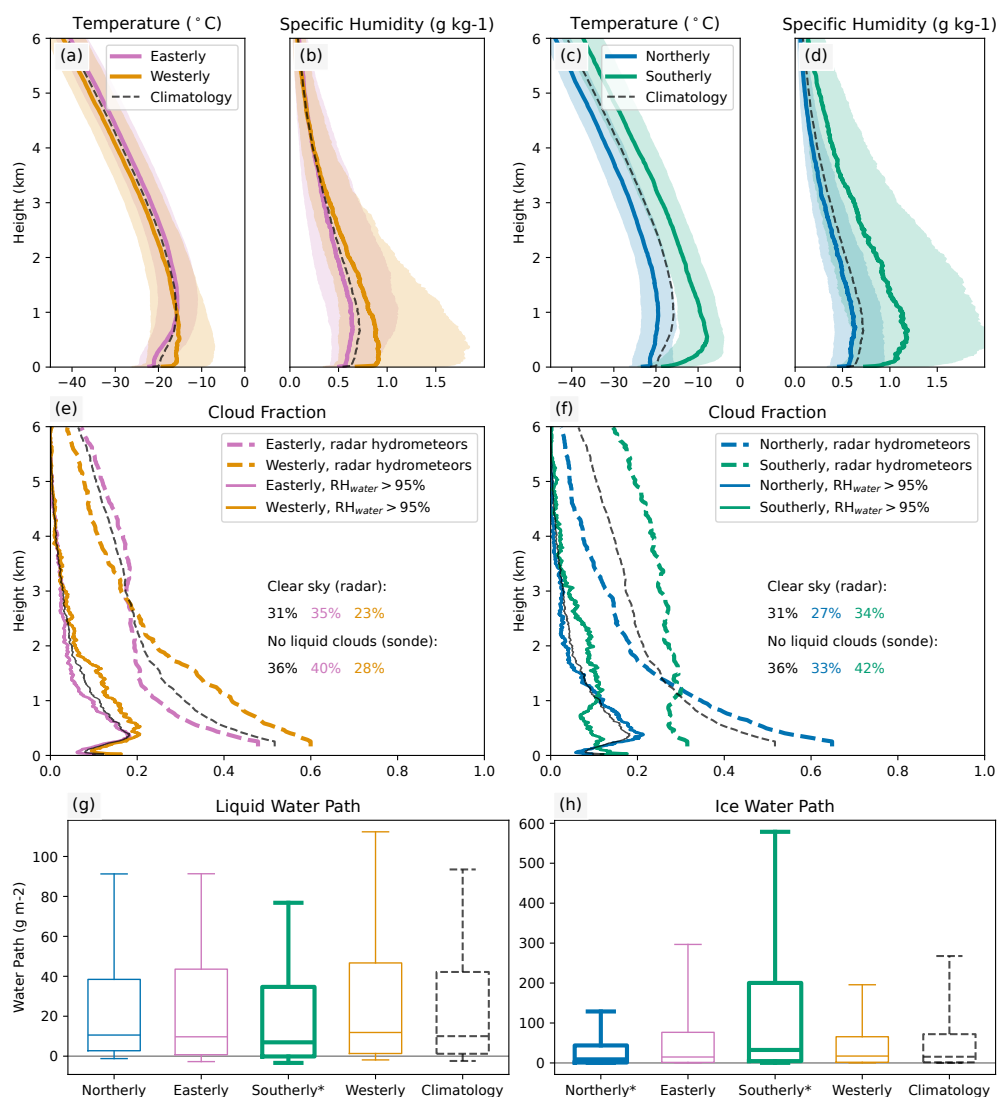


Figure 4. Despite differences in meteorological and other cloud properties, most wind directions produce statistically indistinguishable liquid water path distributions. Panels compare conditions during easterly (45° to 135°; in pink) and westerly (225° to 315°; in orange) winds (panels a, b, e, g) and between northerly (315° to 45°; in blue) and southerly (135° to 225°; in green) winds (panels c, d, f, h) at 500 m at North Slope of Alaska: temperature (a, c) and specific humidity (b, d) profiles; vertical profiles of cloud fraction from the radar (e, f; dotted lines) and liquid cloud fraction from soundings (solid lines); box-and-whisker plots of liquid (g) and ice (h) water path, excluding radar-detected clear sky cases. Shaded regions correspond to the 25th to 75th percentile range (a-d). Saturated regions (e, f) are defined as RH>95% in soundings. Box-and-whisker plots (g, h) are bolded and labeled with an asterisk if the distribution is significantly different from climatology, and whiskers extend to the 10th and 90th percentiles. Black dashed lines in all panels are all-winter climatology, while the black solid line in (e, f) is climatology for the RH>95% condition.



Wind direction at NSA serves as a simple first step towards classifying by meteorological regimes. The climatology of wind direction at 500 m, near the mean liquid-containing cloud base height, is bimodal, with one peak for easterly winds and another for westerly winds (Fig. A6). Defining each wind category as a 90° slice centered on 0 (Northerly), 90 (Easterly), 180 (Southerly), or 270° (Westerly), Fig. 4 compares these four regimes across multiple observation metrics. Wind direction regimes carry marked differences in both meteorology and cloud properties. Westerly and southerly conditions are both warmer and moister than climatology over at least the bottom kilometer, where most liquid-containing clouds are located according to panels (c) and (d). This is true also for the subset of times that contain liquid-containing clouds (Fig. A7). Easterlies have a lower cloud fraction (panels (e) and (f), where cloud fraction is all radar-detected hydrometeors) near the surface, being generally colder and drier there, but so do southerlies despite being both warm and moist. However, despite these substantial differences in temperature, moisture, cloud fraction, and even liquid cloud fraction, the wind-dependent behavior of cloud condensed water paths is unique and even appears inconsistent with other properties. Liquid water path distributions for northerlies, easterlies, and westerlies are not significantly different from climatology. Despite being the warmest and moistest wind direction, southerlies are associated with the statistically lowest liquid water path distribution. Additionally, these southerlies have much larger ice water paths while northerly winds, which are much colder, have the lowest ice water paths, both of which are significantly different from climatology. Thus, liquid water path is not strongly controlled by the many factors that vary with wind direction and do lead to differences in other cloud and atmospheric properties.

3.4 The large-scale circulation perspective

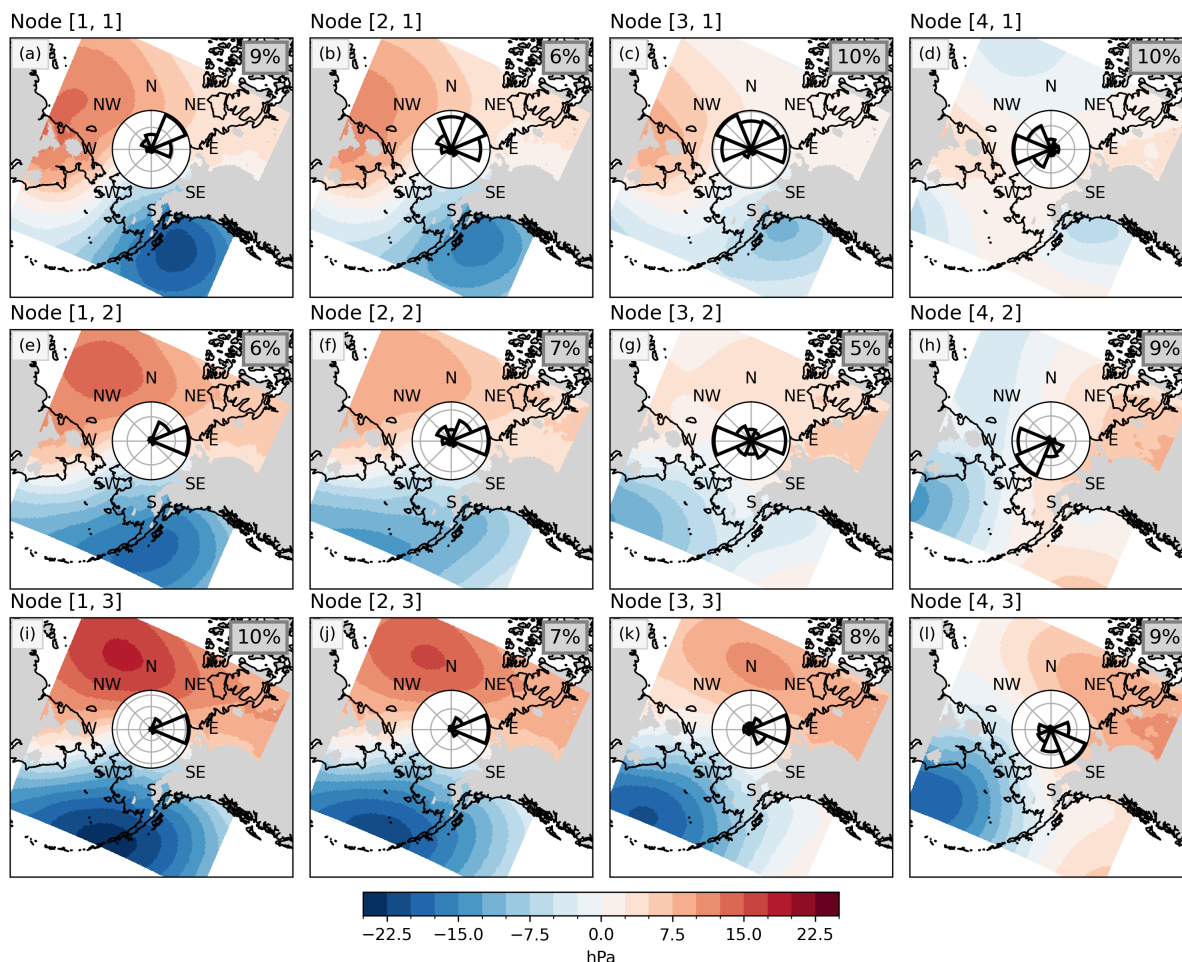


Figure 5. Self-organizing maps (SOM) show the correspondence between sea level pressure anomalies and 500 m wind direction at North Slope of Alaska. Shaded contours show the sea level pressure anomaly of each map node while a wind rose gives the distribution of 500 m wind direction according to sondes at North Slope of Alaska during each node. The frequency of each node from 2011-2023 is given in the upper right-hand corner.

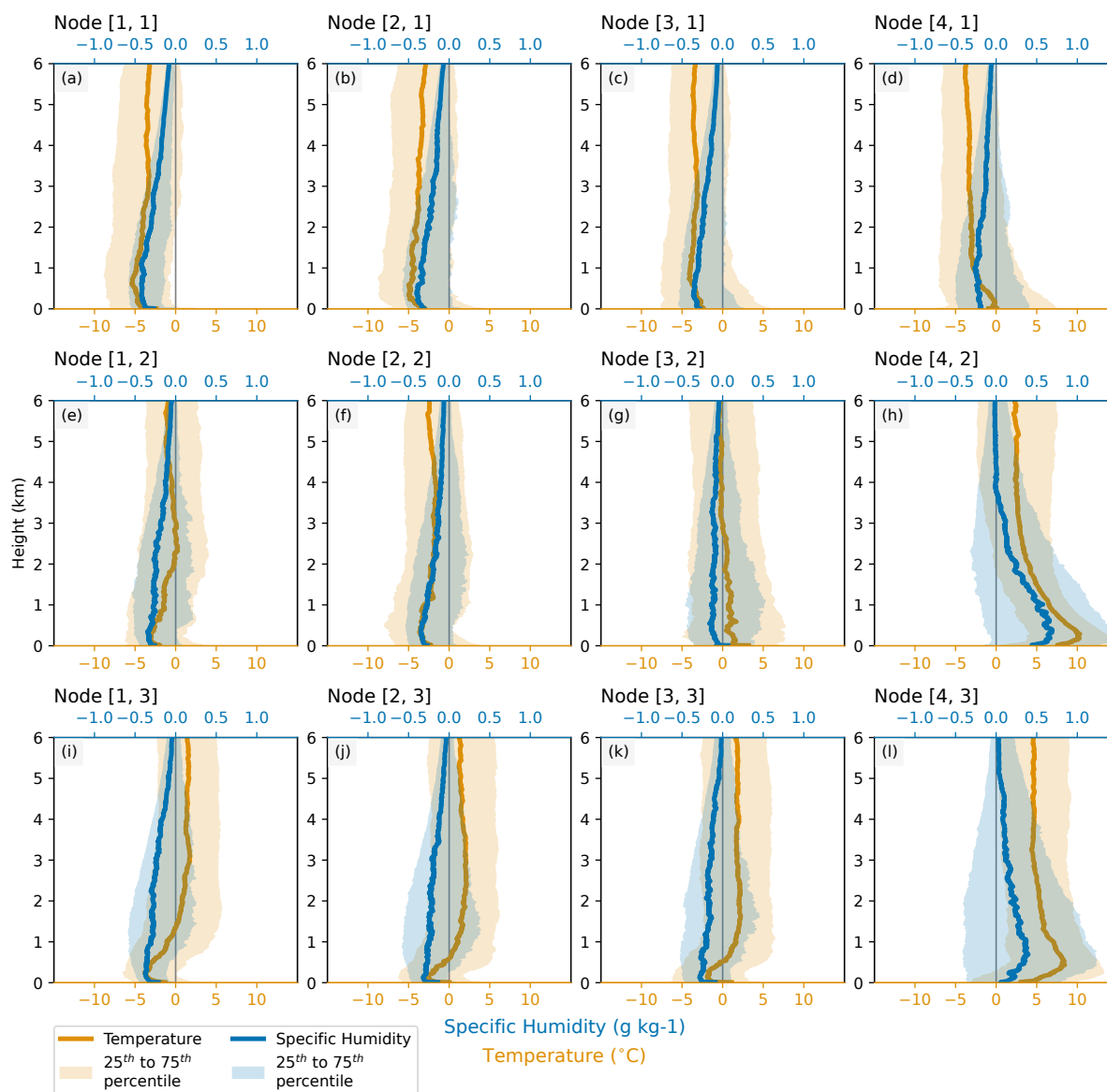


Figure 6. SOMs generate nodes with distinct meteorological conditions. Vertical profiles are shown for the difference between conditions during each node and climatology for temperature (gold) and specific humidity (blue). For each node, the median (solid line) and 25th to 75th percentile (shaded region) of anomalies from climatology are represented. The lower x-axis gives temperature in degrees Celsius while the upper x-axis shows specific humidity in g/kg; both axes scales are the same for all panels. The node label is given above each plot, and the positions within the grid are the same as in Fig. 5.



To better capture aspects of the regional air mass history, we turn to self-organizing maps (SOM) to classify the 6-hourly sea level pressure anomalies around the North Slope into a series of 12 nodes. The sea level pressure anomalies and corresponding wind directions at 500 m at NSA are shown in Fig. 5, while Fig. 6 shows the associated temperature and moisture anomalies. Each panel corresponds to a single SOM node, displayed in the same location in both figures, with the corresponding wind direction, temperature, or moisture taken from all soundings at times when the large-scale circulation was identified to be within that node. The SOM nodes meaningfully capture significant variations in wind direction, temperature, and moisture at NSA, providing a useful classification of meteorological regimes. Variations in sea level pressure anomaly are primarily expressed through the strength and positioning of the Beaufort High-Aleutian Low dipole, which is a characteristic feature of the wintertime circulation in this region. There is fairly close correspondence between large-scale circulation and wind direction at NSA, with the primary wind direction rotating counter-clockwise about the wind rose as one proceeds clockwise around the SOM. A strong Beaufort high in the lower left corner corresponds to easterly winds, with dry air coming out of the Central Arctic and northern Canada that produces a cold anomaly near the surface but a warm anomaly aloft. The SOM transitions to northeasterly winds in the upper left corner, bringing uniformly cold and dry air masses from the Central Arctic. In the upper right corner are weaker pressure anomalies with assorted but mostly westerly winds, bringing air out of Russia and the Central Arctic. The lower right corner features air masses arriving on southerly winds out of the North Pacific with surface-amplified warm and moist anomalies. As is characteristic of a SOM analysis, the most similar sea level pressure patterns are nearest each other while the most different are furthest apart. The smooth variation in corresponding temperature and moisture anomalies across the SOM space indicates that they tend to vary in consistent ways with the large-scale circulation.

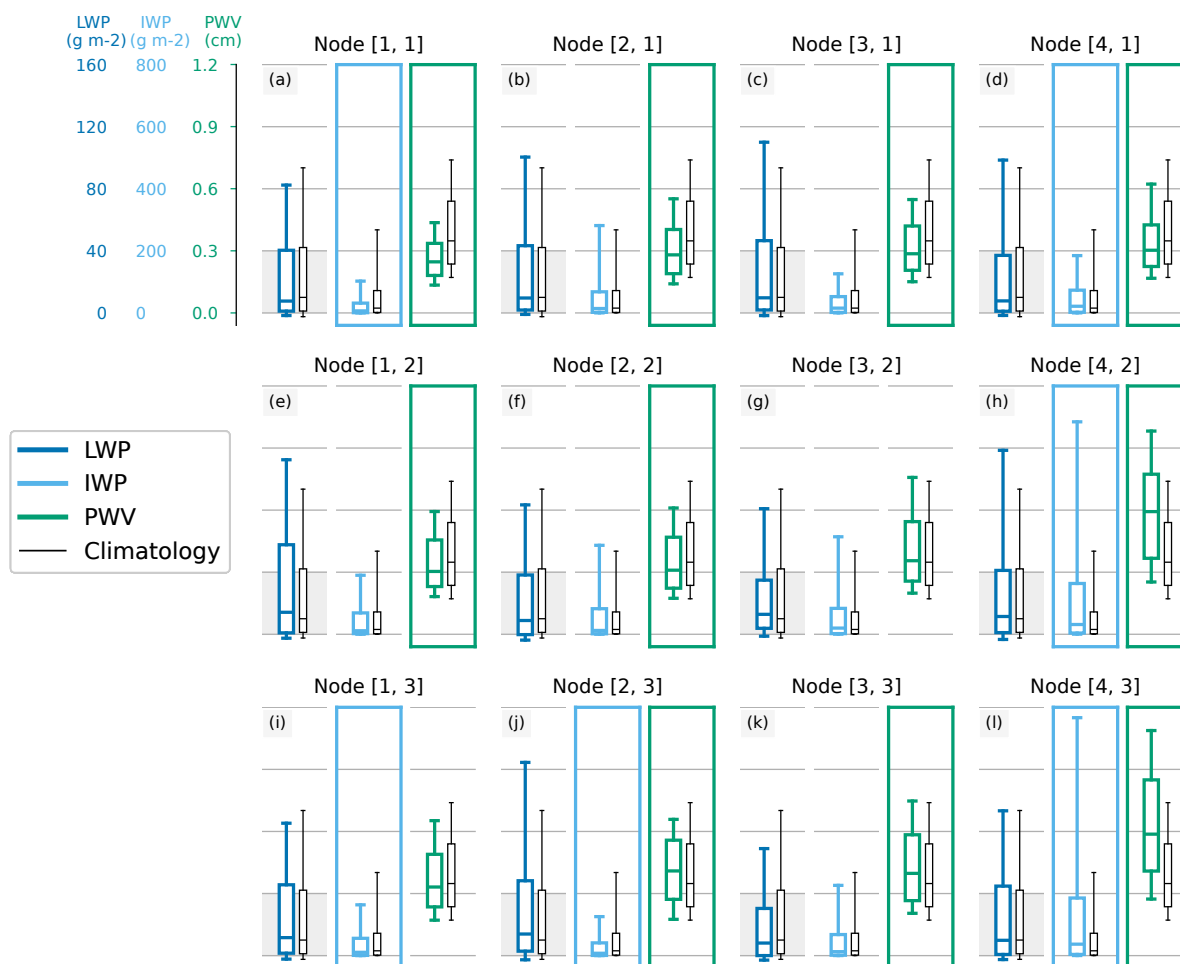


Figure 7. Liquid water path distributions during each of the large-scale circulation regimes characterized by SOMs are statistically indistinguishable from the climatological distribution while ice water path and precipitable water vapor vary significantly. Each node panel contains three box-and-whisker plots with whiskers out to the 10th and 90th percentiles of liquid water path (dark blue) on the left, ice water path (light blue) in the middle, and precipitable water vapor (green) on the right. The black plots are all-winter climatology and therefore the same for all nodes. If the distribution for a given node is significantly different from climatology, that plot is outlined in the corresponding color.



While total atmospheric moisture and cloud ice also tend to vary significantly with the large-scale circulation, liquid water path does not. Figure 7 shows the liquid water path, ice water path, and precipitable water vapor distributions for each SOM node compared to their climatological distributions. As expected, most nodes have a precipitable water vapor that is significantly different from climatology, marked by a green outline, demonstrating that total atmospheric moisture is highly constrained by the large-scale circulation. Additionally, half of the nodes have significant differences in ice water path, marked by a light blue outline. To the extent that SOM nodes represent meteorological regimes, moisture therefore varies consistently with meteorology and ice water path responds to those variations. However, not a single node has a liquid water path distribution that is statistically distinguishable from climatology. Even the warm and moist nodes in the lower right corner, which have the highest occurrence of the highest percentile bins of precipitable water vapor from Fig. 3 and notably high ice water path, show only statistically insignificant variations from the climatological liquid water path distribution. Adjacent nodes, which have the most similar circulation, temperature, and moisture, do not even deviate from climatology in the same direction; just compare [1, 1] to [1, 2], or [3, 1] to [4, 1]. On the whole, the meteorology itself and even cloud ice water path show significant sensitivities to the large-scale circulation regime. By contrast, liquid water path is remarkably insensitive to large-scale circulation, with similar circulation regimes producing different and, ultimately, insignificant liquid water path anomalies.

330 4 Discussion

Using over ten years of observations from multiple ground-based instruments coordinated with radiosondes at NSA in winter, this study probed relationships between meteorological conditions and cloud phase with a particular focus on cloud liquid water path. Beginning with simple assumptions about how cloud base conditions and air mass history might influence cloud phase, we sought to understand the extent to which variations in these conditions could explain the overall distribution of cloud liquid and ice water path. Surprisingly, we found that while ice water path scales with bulk atmospheric moisture, liquid water path is remarkably insensitive to meteorology and large-scale circulation, raising questions about the fundamental processes governing liquid-containing cloud layers, interactions between cloud ice and cloud liquid, and how the coupled Arctic system will respond to a warming climate.

The results presented throughout this study suggest two key conclusions that begin to shape the path for further investigation. First, liquid water path is relatively insensitive to cloud base temperature in the temperature ranges most relevant to wintertime Arctic mixed-phase clouds. This can be seen directly for cases with a single liquid-containing layer shown in Fig. 2, where cloud base temperatures from -25 to -5°C , which accounts for about three-quarters of all liquid-containing clouds at NSA, allow for any liquid water path from optically thin to optically thick. Second, both low and high liquid water path frequencies are largely insensitive to changes in meteorological regime. The liquid water path distribution is statistically indistinguishable across meteorological regimes as defined by either 500 m wind direction (Fig. 4) or by SOM nodes (Fig. 7). Ultimately, neither cloud base temperature nor wind direction nor large-scale circulation regime appear to be reliable predictors of liquid water path.



A more robust indicator, one with a somewhat clearer relationship with cloud liquid and cloud ice than wind direction or large-scale circulation, is precipitable water vapor. Ice water path increases monotonically with precipitable water vapor while liquid water path increases up to the 60th percentile of PWV before leveling off (Fig. 3 and A4). However, just because specific precipitable water vapor ranges have significant differences in cloud liquid water path does not appear to mean that changes in precipitable water vapor distribution lead to changes in liquid water path distribution. As evidence, consider cloud and atmospheric water vapor distributions distinguished by SOM node in Fig. 7, where many nodes have a precipitable water vapor or ice water path distribution significantly different from climatology but none has a significantly different liquid water path distribution. Two factors appear to be at work here. On the one hand, all but the very highest precipitable water vapor bins still have less than 20 g m⁻² of either ice or liquid in the majority of cases (Fig. 3), so high water vapor is not a guarantee of high condensed water path. On the other hand, while some circulation regimes are more likely to bring high precipitable water vapor, they do not exclusively do so. About half of all cases for the two moistest SOM nodes have precipitable water vapor below the 75th percentile of climatology for PWV. Taken together, the relatively modest increase in liquid water path with PWV (Fig. 3) plus the wide range of PWV for any given SOM node (Fig. 7) means that even the circulation regimes favorable to high precipitable water vapor do not necessarily lead to high liquid water path.

Throughout these results, the Clausius-Clapeyron relationship emerges as a strong constraint on cloud liquid water path in a way that is perhaps counter-intuitive. First, as long as an air mass is on or near the saturation curve, any cooling supports cloud formation. The exponential relationship between temperature and moisture at saturation requires more cooling with a colder initial temperature at the same relative humidity, but saturation is always accessible, as evidenced by the consistency of the liquid water path distribution even during colder, drier conditions such as northerly winds (Fig. 4) and SOM nodes [1, 1] and [2, 1] (Figs 6 and 7). Second, warm and moist air masses are not necessarily any closer to saturation than cold and dry ones as long as moisture is measured in absolute terms. If the excess moisture is not sufficient to compensate for the excess temperature, then warmer and moister conditions will not necessarily bring more cloud liquid, as seen in the lack of response of the liquid water path distribution to meteorological conditions with high moisture in Figs 3, 4, and 7.

We next propose a collection of key processes that could explain the unexpected insensitivity of cloud liquid water to meteorology and large-scale circulation observed in this study. Preliminary support for some processes can be found in the figures above, and particularly in the Appendices, but all will require further analysis to either validate or discard.

Hypothesis 1: Continuous radiative cooling and a lack of dissipative mechanisms allow low liquid water path clouds to form often and persist for long periods of time, as suggested by Herman and Goody (1976). The prevalence of clouds with low liquid water path may simply be a consequence of a lack of dissipative mechanisms in a highly stratified environment and continuous air mass cooling. Many of the dissipative mechanisms active at lower latitudes are much weaker in the Arctic in winter. Cloud-top entrainment can actually work to maintain rather than dissipate cloud layers, as humidity inversions are common in the Arctic and cause entrainment to bring in moister rather than drier air (Solomon et al., 2011). There are fewer INPs than at lower latitudes, decreasing the efficiency of ice processes. Weak surface fluxes and strong boundary layer stability often decouple Arctic cloud layers from the surface, insulating them from surface turbulence and aerosols. Meanwhile, radiative cooling continuously drives air masses towards the saturation point and condensation. In this framework, typical conditions



favor cloud persistence until either external forcings disrupt it or precipitation has removed sufficient moisture that further cooling is insufficient to bring the air mass to saturation. This persistence of low LWP clouds is seen in the consistency of the liquid water path distribution across all SOM nodes (Fig. 7) and the two predominant wind directions (Fig. 4), suggesting similar cloud LWP regardless of circulation regime or moisture availability.

Hypothesis 2: Competing temperature dependencies among ice processes contribute to a flat temperature response for liquid water path at intermediate supercooled temperatures. At colder temperatures, ice nucleation is more efficient, with more INPs active as the temperature decreases (DeMott et al., 2016; Wex et al., 2019; Creamean et al., 2022; Gjelsvik et al., 2025), but water vapor is scarce, allowing for primarily low liquid water paths. At intermediate temperatures, around -12°C , the difference between saturation vapor pressure over liquid and ice is maximized (Korolev and Isaac, 2003) and water vapor is more plentiful, producing a wide range of liquid and ice water paths. At warmer temperatures, water vapor becomes more prevalent, supporting more rapid ice growth to compete with the liquid via WBF and the seeder-feeder mechanism. Yet ice nucleation itself becomes less effective because there are relatively few warm temperature INPs (Creamean et al., 2022), while some proposed secondary ice processes might become more effective at relatively warmer temperatures (Korolev and Leisner, 2020; Field et al., 2017). Competing tendencies at all temperatures could produce the observed insensitivity of the liquid water path distribution at all but the warmest and coldest supercooled temperatures.

Hypothesis 3: The efficiency of ice production depends on the amount and properties of cloud liquid, limiting the highest liquid water amounts. Once ice appears in a supercooled liquid-containing cloud, it efficiently converts liquid mass to ice mass via the WBF process. Additionally, there are a collection of ice production mechanisms that should, in theory, increase as liquid water path increases. In the relatively clean air of the Arctic, a cloud condensation nuclei (CCN)-limited regime implies that a higher condensed liquid mass results in larger rather than more numerous liquid droplets. Higher liquid water path therefore implies more liquid mass and more large liquid droplets, both of which can enhance ice nucleation, secondary ice production, and/or riming (Lauber et al., 2018; Korolev and Leisner, 2020). In this framework, cloud layers with a very low liquid water path, like those so commonly observed across the Arctic, would be poor ice-producers, shutting down one of the main dissipative mechanisms and allowing these clouds to form and persist relatively easily. A cloud layer with higher liquid water path, on the other hand, would also efficiently produce and grow ice that competes with the liquid and limits further liquid mass production. Indicators of such a feedback appear in this study in the response of cloud water to precipitable water vapor in the highest few percentile bins, as liquid water path levels off even as ice water path increases sharply.

Hypothesis 4: When there is high precipitable water vapor, it often involves deep layers of enhanced moisture leading to enhanced ice production aloft that activates the seeder-feeder mechanism, limiting the expected increase in liquid water path. Above the 90th percentile of precipitable water vapor, the largest water vapor anomalies are between 500 and 1,500 meters, which is located above the peak in liquid-containing cloud fraction at 350 meters (Fig. A8). This indicates that much of the excess water vapor is above liquid-containing cloud layers and thus may instead contribute directly to enhanced ice production. The median anomaly in relative humidity for the highest PWV bin exceeds 20% from 2 km to above 6 km, providing a considerable vertical distance through which ice can form, grow, and fall. Accordingly, we found that the total mass of ice above the highest liquid-containing layer increases with precipitable water vapor, with a particularly sharp increase for the



highest PWV percentile bin (Fig. A9), supporting the stronger correspondence between ice water path and precipitable water vapor. The same relationship can be seen in southerly winds, which bring enhanced moisture and cloud fraction aloft but lower liquid water path and liquid-containing cloud fraction in the bottom kilometer of the atmosphere (Fig. A6). The increase in ice mass aloft can also be shown to coincide with an increase in ice precipitation into liquid-containing layers: the fraction of all liquid-containing layers that have radar-detected hydrometeors directly above them, presumably precipitating ice, also increases from 56% to 69% from the 50th to the 90th percentile bin of precipitable water vapor (Fig. A10).

The result of these competing dependencies might help explain the observations from NSA, with low liquid and ice water paths under the very coldest and driest conditions, a relatively flat response to temperature as ice processes compete at intermediate temperatures, and high ice water paths that damp some of the expected increase in liquid water path under warm and moist conditions. As these hypotheses are supported by some information but not rigorously tested, more detailed analysis of, for example, the temperature dependence of ice production and co-evolution of liquid and ice within clouds is needed to investigate these claims.

5 Conclusions

Liquid water path in Arctic winter is largely insensitive to temperature, moisture, winds, and large-scale circulation. This study uses over ten years of continuous observations from NSA across multiple instruments to investigate the correspondence between cloud liquid, cloud ice, and meteorological conditions. Radiosonde soundings, cloud radar, ceilometer, and microwave radiometer generally agree that liquid-containing clouds are present 60-70% of the time at NSA between November and March. At cloud base temperatures between -25 and -5°C, encapsulating about three-quarters of all wintertime liquid-containing clouds, a broad range of liquid water paths are accessible. Cloud ice responds strongly but liquid weakly to precipitable water vapor, particularly at the highest percentiles of available moisture. Meteorological regimes, whether defined by local wind direction or large-scale circulation, come with distinct temperature, moisture, and cloud ice conditions, but all produce statistically similar liquid water path distributions.

The remarkable persistence yet apparent insensitivity of wintertime liquid-containing clouds calls for new ideas and methods as well as revisiting older frameworks. We propose a collection of hypotheses consistent with the observations presented here, centered primarily around the continuous radiative cooling of air masses and the role of ice in enabling or limiting liquid mass accumulation. We encourage the community to challenge them with observational data and targeted model studies. A focus on dissipative mechanisms is warranted, and particularly on the conditions that limit them in many cases. An air mass transformation approach could begin to untangle what causes liquid water path to increase or decrease throughout the air mass lifecycle, although acquiring high-fidelity information on cloud water properties at sufficient spatial and temporal resolution for such an analysis remains a major technical challenge. An investigation into whether the relationships found in this study between temperature, moisture, circulation, and cloud ice and liquid water path hold at other Arctic locations or in models could also help gauge the universality of Arctic cloud properties and their implications for climate. Whatever the method, any answers to the many questions raised by these results would represent a significant step forward in our understanding of Arctic



cloud properties, how they could be better represented in models, and how they might respond to changing meteorological conditions.

Code and data availability. Data were obtained from the Atmospheric Radiation Measurement (ARM) User Facility, a U.S. Department of Energy (DOE) Office of Science user facility managed by the Biological and Environmental Research Program. All datasets are available
455 for download at <https://adc.arm.gov/discovery/> under the following datastreams: nsaceilC1.b1 (Zhang et al., 1997), nsamwrret1liljclouC1.c2 (Zhang, 2001), nsasondownpnC1.b1 (Keeler et al., 2002), nsakazrcorgeC1.c1 (Johnson et al., 2011), nsakazrcorgeC1.c0 (Johnson et al., 2014), and nsakazrcfrorgeC1.c0 (Toto and Giangrande, 2019). The code used to process these datasets, perform the analysis, and generate all figures can be found at DOI 10.5281/zenodo.19197511 (Hartig, 2026).

Appendix A

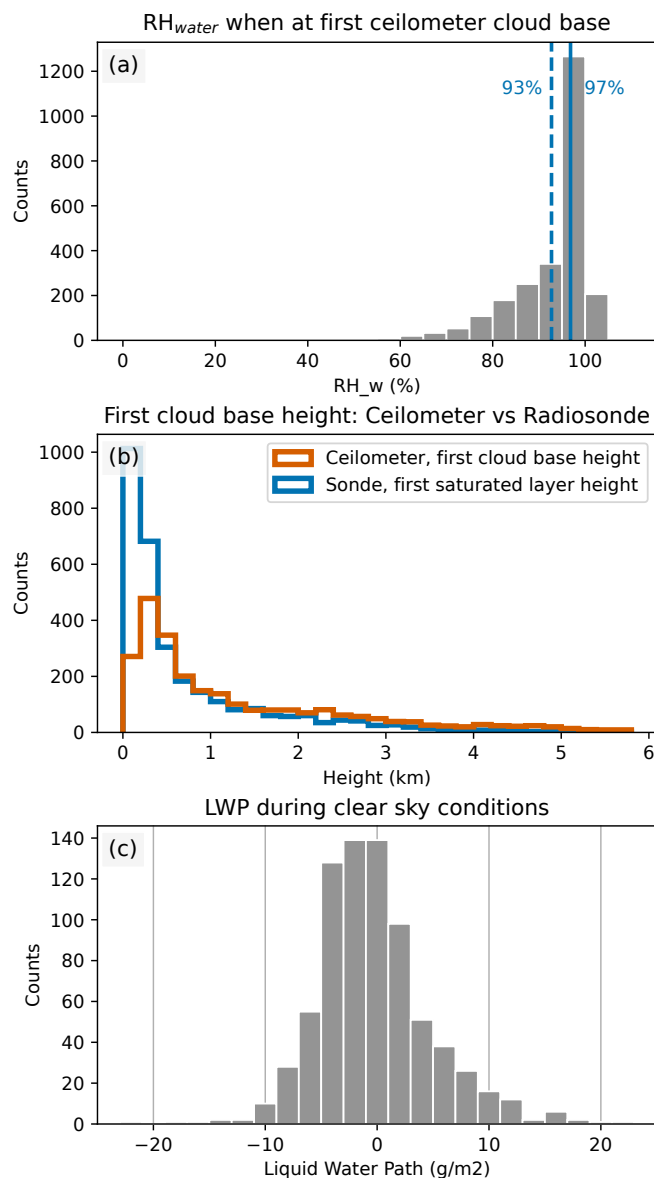


Figure A1. (a) Relative humidity with respect to liquid water from the radiosonde at the first cloud base height detected by the ceilometer. The blue dashed line and accompanying text indicate the mean of the distribution, while the blue solid line indicates the median. (b) Liquid water path distribution during clear sky conditions. (c) First cloud base height from the ceilometer (rust) and the base of the first saturated layer from the radiosonde (blue).

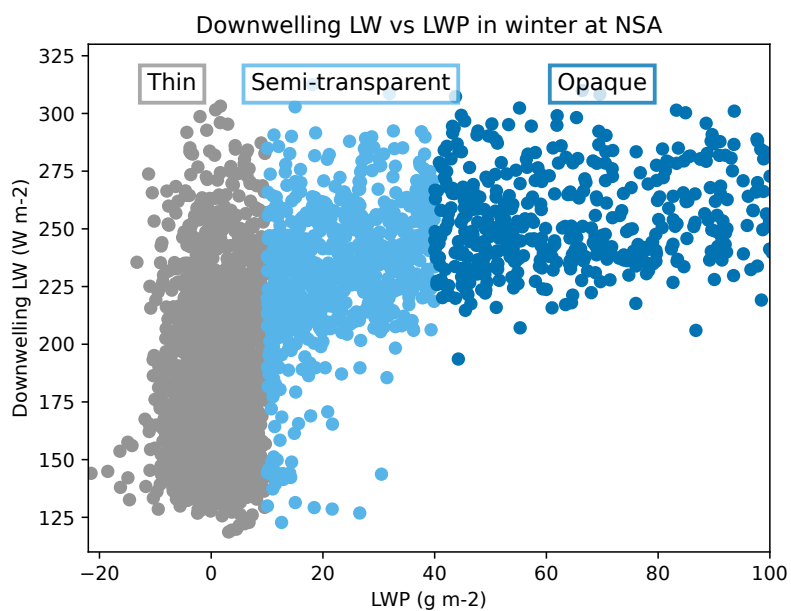


Figure A2. Downwelling longwave radiation at the surface as a function of liquid water path. Points are colored according to the three liquid water path categories defined in the paper: Thin ($<10 \text{ g m}^{-2}$), Semi-transparent ($10\text{--}40 \text{ g m}^{-2}$), and Opaque ($>40 \text{ g m}^{-2}$). Downwelling longwave radiation is the downwelling longwave hemispheric irradiance reported in the qcrad1long.c2 datastream.

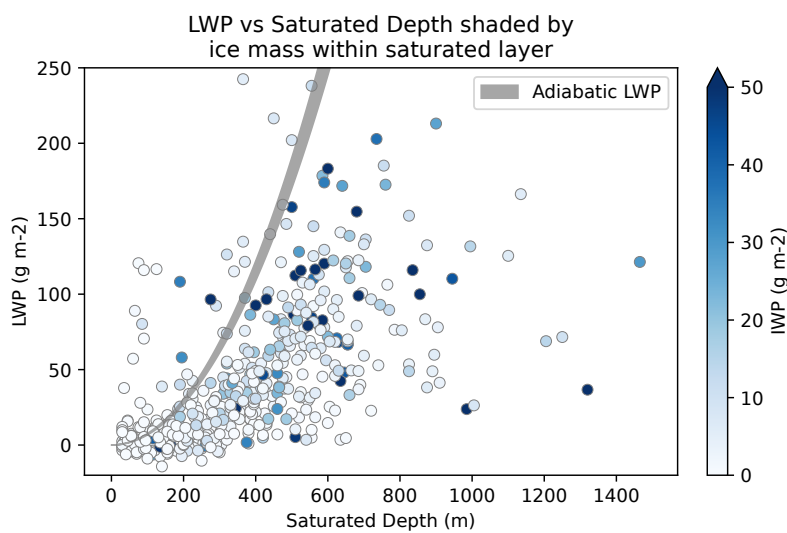


Figure A3. Liquid water path as a function of saturated depth for cases with a single saturated layer and a cloud base temperature between -20 and -10 degrees C, colored by the amount of ice within the saturated layer. The grey shaded region shows the adiabatic liquid water path predicted as a function of saturated depth for cloud base temperatures between -20 and -10 degrees C. Displays the same cases as in Figure 2b of the main manuscript.

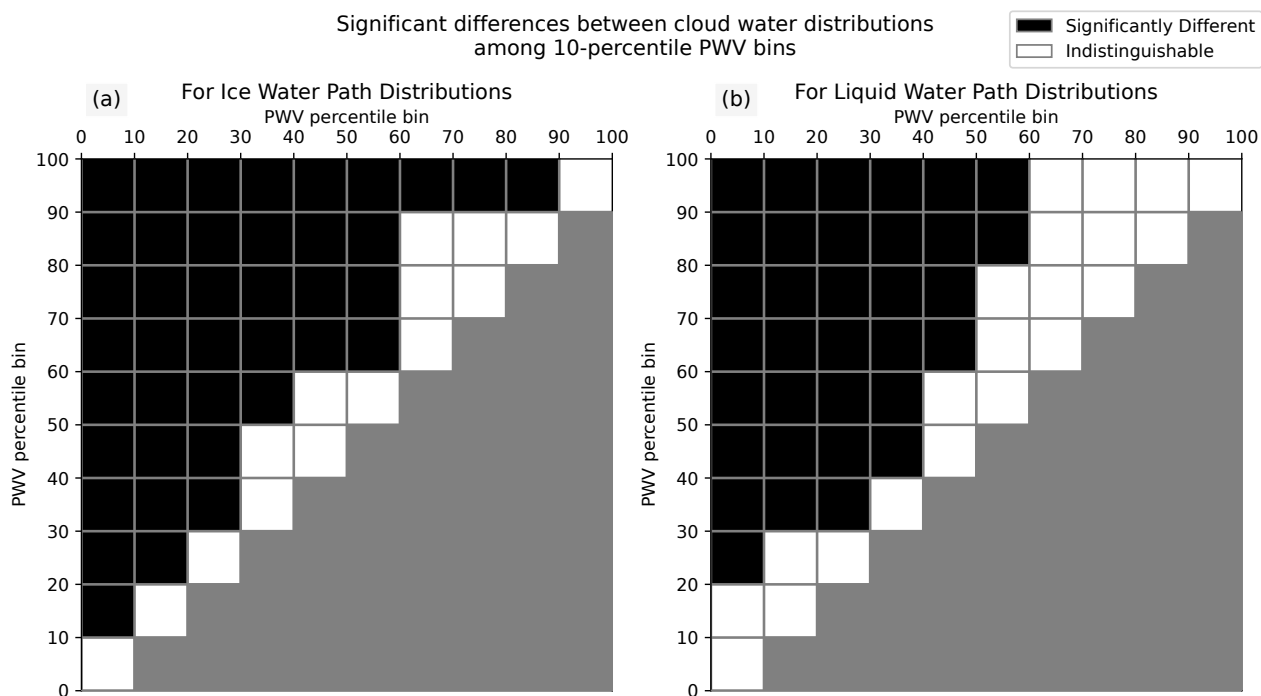


Figure A4. Significant difference flags between all pairs of ice (a) and liquid (b) water path distributions by PWV percentile from Figure 3. Significant difference is determined at the 95% level by a two-sample Kolmogorov-Smirnov test.

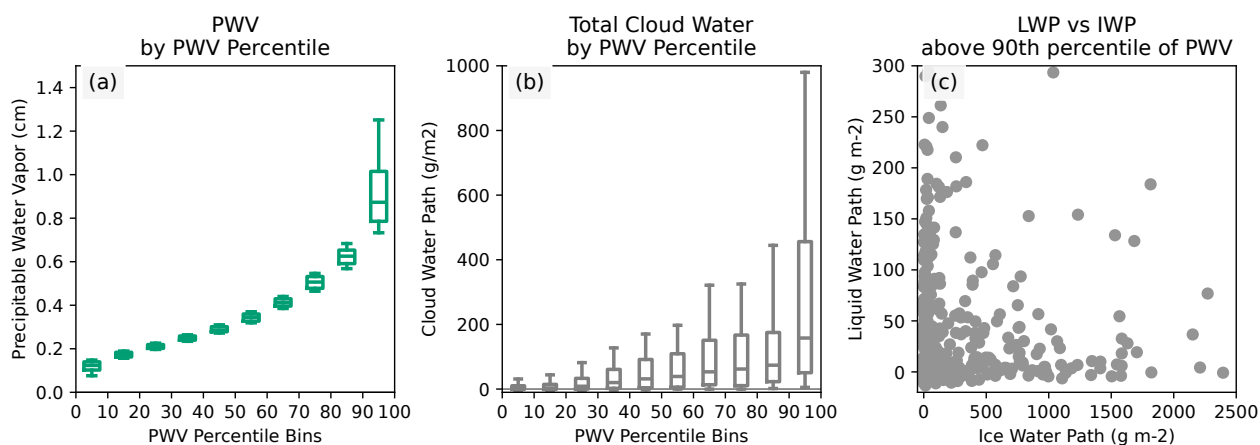


Figure A5. Box-and-whisker plots of precipitable water vapor (a) and total cloud water (ice water path plus liquid water path) (b) by precipitable water vapor percentile as well as the correspondence between liquid and ice water path for the highest precipitable water vapor bin (c). The whiskers in (a) and (b) extend to the 10th and 90th percentiles.

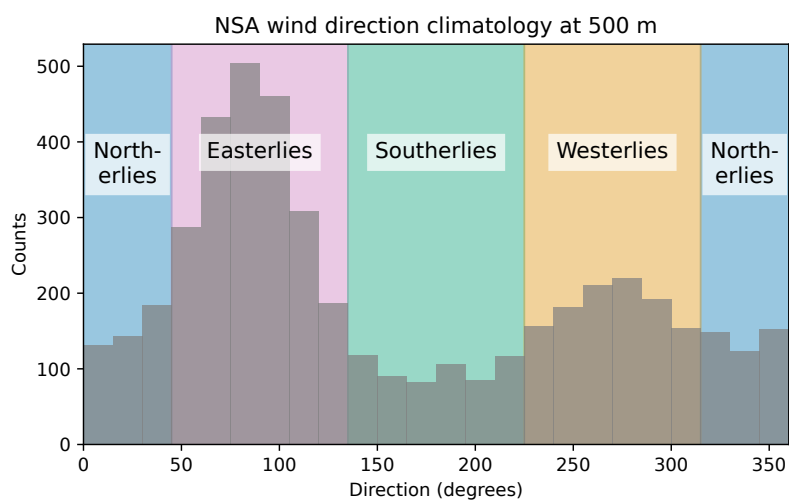


Figure A6. The distribution of 500 m wind direction at NSA, with the ranges defining northerlies (blue), easterlies (pink), southerlies (green), and westerlies (orange) shaded.

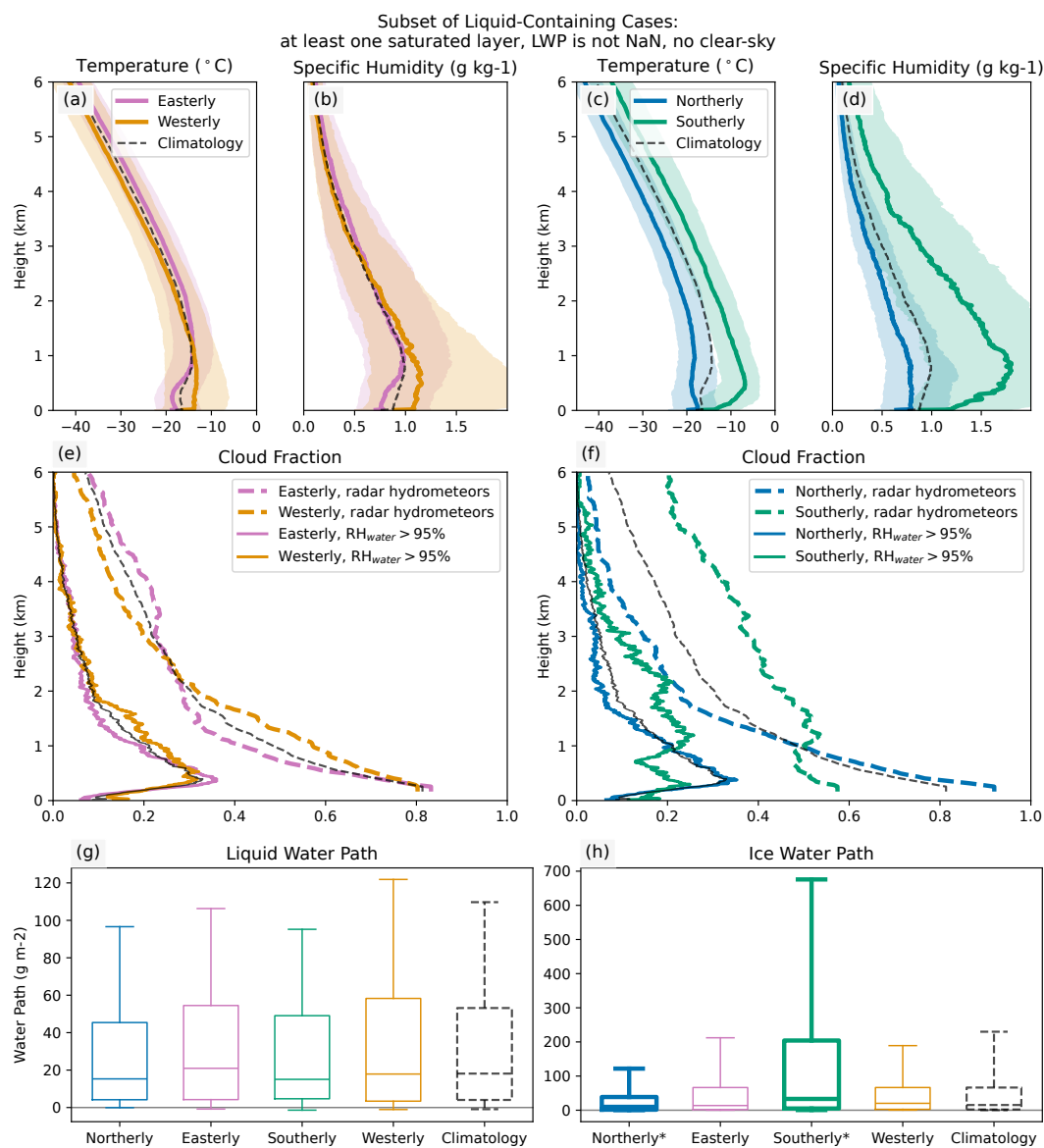


Figure A7. Same as Figure 4 in the main manuscript, except all panels display the same subset of cases: at least one saturated layer is present, the liquid water path is defined, and the radar does not detect clear sky.

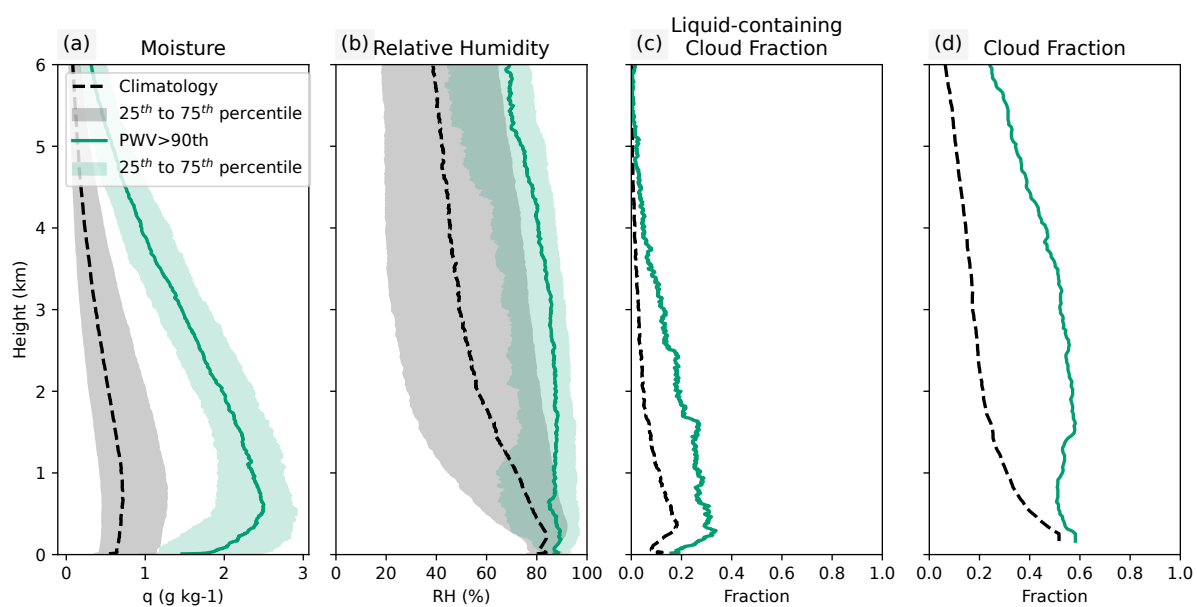


Figure A8. Comparing climatological vertical profiles (in black) of specific humidity (a), relative humidity (b), saturated layer fraction (c), and cloud fraction (d) to those when PWV is above its 90th percentile (in green). Shaded regions demarcate the 25th to 75th percentile range over all cases while solid and dashed lines indicate the median.

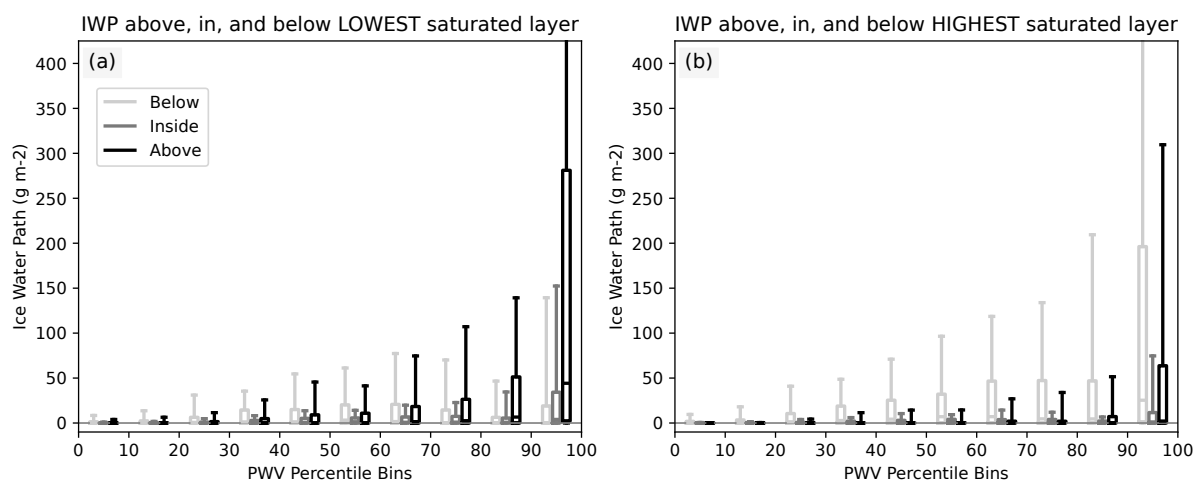


Figure A9. Distributions, by PWV percentile bin, of the total ice water path above (black), inside (grey), and below (light grey) the lowest (a) and highest (b) saturated layer.



What fraction of HIGHEST saturated layers have hydrometeors directly above?

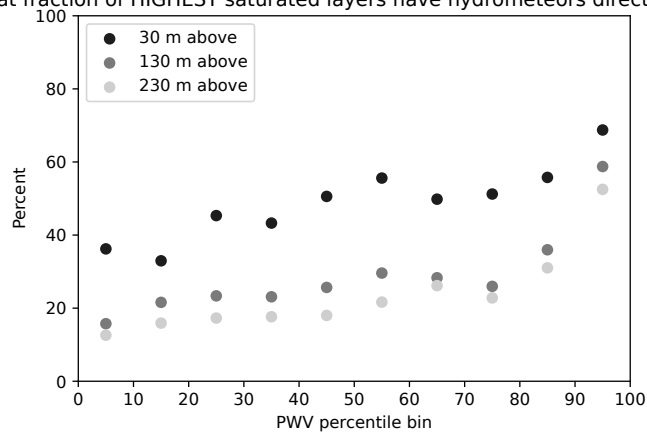


Figure A10. Fraction of the highest saturated layers, by PWV percentile bin, that have radar-detected hydrometeors at three heights directly above saturated layer top.



460 *Author contributions.* All authors conceptualized the core ideas and provided input throughout their development and the analysis. KH processed the data, performed the analysis, and prepared the manuscript, with reviewing and editing contributions from all co-authors.

Competing interests. The authors declare that they have no conflict of interest.

Acknowledgements. KH was supported by the CIRES Visiting Fellows Program, funded by NOAA Cooperative Agreement NA22OAR4320151, and by the U.S. National Science Foundation Office of Polar Programs under Award No. 2420081. This research was supported in part by
465 grant NSF PHY-2309135 to the Kavli Institute for Theoretical Physics (KITP). JJC was supported by the Regional and Global Modeling Analysis (RGMA) component of the Earth and Environmental System Modeling (EESM) program of the U.S. Department of Energy's Office of Science, as a contribution to the HiLAT-RASM project (contract no. DE-SC0024872). MDS was supported by the NOAA Global Ocean Monitoring and Observing Program (FundRef <https://doi.org/10.13039/100018302>) and NOAA Cooperative Agreement (NA22OAR4320151). AS was supported by NASA Award No. 80NSSC22K1775.



470 References

- Achtert, P., Seelig, T., Wallentin, G., Ickes, L., Shupe, M. D., Hoose, C., and Tesche, M.: Occurrence of seeding multi-layer clouds in the Arctic from ground-based observations, *Atmospheric Chemistry and Physics*, 26, 3049–3068, <https://doi.org/10.5194/acp-26-3049-2026>, 2026.
- Ali, S. M. and Pithan, F.: Following moist intrusions into the Arctic using SHEBA observations in a Lagrangian perspective, *Quarterly Journal of the Royal Meteorological Society*, 146, 3522–3533, <https://doi.org/10.1002/qj.3859>, 2020.
- Bergeron, T.: Procès Verbaux de l'Association de Météorologie, International Union of Geodesy and Geophysics, pp. 156–178, 1935.
- Bertossa, C. and L'Ecuyer, T.: Two Ubiquitous Radiative States Observed across the High Latitudes, *Journal of Climate*, 37, 2585–2610, <https://doi.org/10.1175/JCLI-D-23-0553.1>, 2024.
- Brodzik, M. J., Billingsley, B., Haran, T., Raup, B., and Savoie, M. H.: EASE-Grid 2.0: Incremental but Significant Improvements for Earth-Gridded Data Sets, *ISPRS International Journal of Geo-Information*, 1, 32–45, <https://doi.org/10.3390/ijgi1010032>, 2012.
- C3S: ERA5 hourly data on single levels from 1940 to present, <https://doi.org/10.24381/CDS.ADBB2D47>, 2018.
- Cadeddu, M. P., Turner, D. D., and Liljegren, J. C.: A Neural Network for Real-Time Retrievals of PWV and LWP From Arctic Millimeter-Wave Ground-Based Observations, *IEEE Transactions on Geoscience and Remote Sensing*, 47, 1887–1900, <https://doi.org/10.1109/TGRS.2009.2013205>, 2009.
- 485 Cadeddu, M. P., Liljegren, J. C., and Turner, D. D.: The Atmospheric radiation measurement (ARM) program network of microwave radiometers: instrumentation, data, and retrievals, *Atmospheric Measurement Techniques*, 6, 2359–2372, <https://doi.org/10.5194/amt-6-2359-2013>, 2013.
- Cai, Z., You, Q., Wu, F., Chen, H. W., Chen, D., and Cohen, J.: Arctic Warming Revealed by Multiple CMIP6 Models: Evaluation of Historical Simulations and Quantification of Future Projection Uncertainties, *Journal of Climate*, 34, 4871–4892, <https://doi.org/10.1175/JCLI-D-20-0791.1>, 2021.
- 490 Cassano, E. N., Lynch, A. H., Cassano, J. J., and Koslow, M. R.: Classification of synoptic patterns in the western Arctic associated with extreme events at Barrow, Alaska, USA, *Climate Research*, 30, 83–97, <https://doi.org/10.3354/cr030083>, 2006.
- Cassano, E. N., Glisan, J. M., Cassano, J. J., Jr, W. J. G., and Seefeldt, M. W.: Self-organizing map analysis of widespread temperature extremes in Alaska and Canada, *Climate Research*, 62, 199–218, <https://doi.org/10.3354/cr01274>, 2015.
- 495 Cesana, G., Kay, J. E., Chepfer, H., English, J. M., and de Boer, G.: Ubiquitous low-level liquid-containing Arctic clouds: New observations and climate model constraints from CALIPSO-GOCCP, *Geophysical Research Letters*, 39, <https://doi.org/10.1029/2012GL053385>, 2012.
- Cox, C. J., Walden, V. P., and Rowe, P. M.: A comparison of the atmospheric conditions at Eureka, Canada, and Barrow, Alaska (2006–2008), *Journal of Geophysical Research: Atmospheres*, 117, <https://doi.org/10.1029/2011JD017164>, 2012.
- Creamean, J. M., Barry, K., Hill, T. C. J., Hume, C., DeMott, P. J., Shupe, M. D., Dahlke, S., Willmes, S., Schmale, J., Beck, I., Hoppe, C. J. M., Fong, A., Chamberlain, E., Bowman, J., Scharien, R., and Persson, O.: Annual cycle observations of aerosols capable of ice formation in central Arctic clouds, *Nature Communications*, 13, 3537, <https://doi.org/10.1038/s41467-022-31182-x>, 2022.
- 500 Cronin, T. W. and Tziperman, E.: Low clouds suppress Arctic air formation and amplify high-latitude continental winter warming, *Proceedings of the National Academy of Sciences*, 112, 11 490–11 495, <https://doi.org/10.1073/pnas.1510937112>, 2015.
- Curry, J. A., Ebert, E. E., and Herman, G. F.: Mean and turbulence structure of the summertime Arctic cloudy boundary layer, *Quarterly Journal of the Royal Meteorological Society*, 114, 715–746, <https://doi.org/10.1002/qj.49711448109>, 1988.
- 505



- Davy, R. and Outten, S.: The Arctic Surface Climate in CMIP6: Status and Developments since CMIP5, *Journal of Climate*, 33, 8047–8068, <https://doi.org/10.1175/JCLI-D-19-0990.1>, 2020.
- De Boer, G., Morrison, H., Shupe, M. D., and Hildner, R.: Evidence of liquid dependent ice nucleation in high-latitude stratiform clouds from surface remote sensors, *Geophysical Research Letters*, 38, n/a–n/a, <https://doi.org/10.1029/2010GL046016>, 2011.
- 510 DeMott, P. J., Prenni, A. J., Liu, X., Kreidenweis, S. M., Petters, M. D., Twohy, C. H., Richardson, M. S., Eidhammer, T., and Rogers, D. C.: Predicting global atmospheric ice nuclei distributions and their impacts on climate, *Proceedings of the National Academy of Sciences*, 107, 11 217–11 222, <https://doi.org/10.1073/pnas.0910818107>, 2010.
- DeMott, P. J., Hill, T. C. J., McCluskey, C. S., Prather, K. A., Collins, D. B., Sullivan, R. C., Ruppel, M. J., Mason, R. H., Irish, V. E., Lee, T., Hwang, C. Y., Rhee, T. S., Snider, J. R., McMeeking, G. R., Dhaniyala, S., Lewis, E. R., Wentzell, J. J. B., Abbatt, J., Lee, C., Sultana, 515 C. M., Ault, A. P., Axson, J. L., Diaz Martinez, M., Venero, I., Santos-Figueroa, G., Stokes, M. D., Deane, G. B., Mayol-Bracero, O. L., Grassian, V. H., Bertram, T. H., Bertram, A. K., Moffett, B. F., and Franc, G. D.: Sea spray aerosol as a unique source of ice nucleating particles, *Proceedings of the National Academy of Sciences*, 113, 5797–5803, <https://doi.org/10.1073/pnas.1514034112>, 2016.
- Doyle, J. G., Lesins, G., Thackray, C. P., Perro, C., Nott, G. J., Duck, T. J., Damoah, R., and Drummond, J. R.: Water vapor intrusions into the High Arctic during winter, *Geophysical Research Letters*, 38, <https://doi.org/10.1029/2011GL047493>, 2011.
- 520 Eytan, E., Koren, I., Altaratz, O., Pinsky, M., and Khain, A.: Revisiting adiabatic fraction estimations in cumulus clouds: high-resolution simulations with a passive tracer, *Atmospheric Chemistry and Physics*, 21, 16 203–16 217, <https://doi.org/10.5194/acp-21-16203-2021>, 2021.
- Field, P. R., Lawson, R. P., Brown, P. R. A., Lloyd, G., Westbrook, C., Moisseev, D., Miltenberger, A., Nenes, A., Blyth, A., Choulaton, T., Connolly, P., Buehl, J., Crosier, J., Cui, Z., Dearden, C., DeMott, P., Flossmann, A., Heymsfield, A., Huang, Y., Kalesse, H., 525 Kanji, Z. A., Korolev, A., Kirchgaessner, A., Lasher-Trapp, S., Leisner, T., McFarquhar, G., Phillips, V., Stith, J., and Sullivan, S.: Secondary Ice Production: Current State of the Science and Recommendations for the Future, *Meteorological Monographs*, 58, 7.1–7.20, <https://doi.org/10.1175/AMSMONOGRAPHS-D-16-0014.1>, 2017.
- Findeisen, W.: Kolloid-meteorologische Vorgänge bei Neiderschlags-bildung, *Meteor. Z.*, 55, 121–133, 1938.
- Francis, J. A. and Hunter, E.: New insight into the disappearing Arctic sea ice, *Eos, Transactions American Geophysical Union*, 87, 509–511, 530 <https://doi.org/10.1029/2006EO460001>, 2006.
- Gallagher, M. R., Shupe, M. D., and Miller, N. B.: Impact of Atmospheric Circulation on Temperature, Clouds, and Radiation at Summit Station, Greenland, with Self-Organizing Maps, *Journal of Climate*, 31, 8895–8915, <https://doi.org/10.1175/JCLI-D-17-0893.1>, 2018.
- Gjelsvik, A. B., David, R. O., Carlsen, T., Hellmuth, F., Hofer, S., McGraw, Z., Sodemann, H., and Storelvmo, T.: Using a region-specific ice-nucleating particle parameterization improves the representation of Arctic clouds in a global climate model, *Atmospheric Chemistry and Physics*, 25, 1617–1637, <https://doi.org/10.5194/acp-25-1617-2025>, 2025. 535
- Graham, R. M., Rinke, A., Cohen, L., Hudson, S. R., Walden, V. P., Granskog, M. A., Dorn, W., Kayser, M., and Maturilli, M.: A comparison of the two Arctic atmospheric winter states observed during N-ICE2015 and SHEBA, *Journal of Geophysical Research: Atmospheres*, 122, 5716–5737, <https://doi.org/10.1002/2016JD025475>, 2017.
- Hartig, K.: LWP_Insensitive_Figures, Zenodo, <https://doi.org/10.5281/zenodo.19197511>, 2026.
- 540 Herman, G. and Goody, R.: Formation and Persistence of Summertime Arctic Stratus Clouds, *Journal of the Atmospheric Sciences*, 33, 1537–1553, [https://doi.org/10.1175/1520-0469\(1976\)033<1537:FAPOSA>2.0.CO;2](https://doi.org/10.1175/1520-0469(1976)033<1537:FAPOSA>2.0.CO;2), 1976.
- Hersbach, H., Bell, B., Berrisford, P., Hirahara, S., Horányi, A., Muñoz-Sabater, J., Nicolas, J., Peubey, C., Radu, R., Schepers, D., Simmons, A., Soci, C., Abdalla, S., Abellan, X., Balsamo, G., Bechtold, P., Biavati, G., Bidlot, J., Bonavita, M., De Chiara, G., Dahlgren,



- P., Dee, D., Diamantakis, M., Dragani, R., Flemming, J., Forbes, R., Fuentes, M., Geer, A., Haimberger, L., Healy, S., Hogan, R. J.,
545 Hólm, E., Janisková, M., Keeley, S., Laloyaux, P., Lopez, P., Lupu, C., Radnoti, G., de Rosnay, P., Rozum, I., Vamborg, F., Vil-
laume, S., and Thépaut, J.-N.: The ERA5 global reanalysis, *Quarterly Journal of the Royal Meteorological Society*, 146, 1999–2049,
<https://doi.org/10.1002/qj.3803>, 2020.
- Hewitson, B. C. and Crane, R. G.: Self-organizing maps: applications to synoptic climatology, *Climate Research*, 22, 13–26,
<https://doi.org/10.3354/cr022013>, 2002.
- 550 Johnson, K., Toto, T., Jensen, M., and Giangrande, S.: KAZR Corrected Data (KAZRCORGE), 2011-11-11 to 2014-02-07, North Slope
Alaska (NSA), Central Facility, Barrow AK (C1), <https://doi.org/10.5439/1228770>, accessed: 2025-02-17, 2011.
- Johnson, K., Toto, T., and Giangrande, S.: KAZR Corrected Data (KAZRCORGE), 2014-02-08 to 2019-10-27, North Slope Alaska (NSA),
Central Facility, Barrow AK (C1), <https://doi.org/10.5439/1389054>, accessed: 2025-01-30, 2014.
- Keeler, E.: Balloon-Borne Sounding System (SONDE) Instrument Handbook, Atmospheric Radiation Measurement (ARM) user facility,
555 2025.
- Keeler, E., Burk, K., and Kyrouac, J.: Balloon-Borne Sounding System (SONDEWNP), 2011-01-01 to 2023-12-31, North Slope Alaska
(NSA), Central Facility, Barrow AK (C1), <https://doi.org/10.5439/1595321>, accessed: 2024-11-12, 2002.
- Kirbus, B., Tiedeck, S., Camplani, A., Chylik, J., Crewell, S., Dahlke, S., Ebell, K., Gorodetskaya, I., Griesche, H., Handorf, D., Höschel, I.,
Lauer, M., Neggers, R., Rückert, J., Shupe, M. D., Spreen, G., Walbröl, A., Wendisch, M., and Rinke, A.: Surface impacts and associated
560 mechanisms of a moisture intrusion into the Arctic observed in mid-April 2020 during MOSAiC, *Frontiers in Earth Science*, 11, 2023.
- Kohonen, T.: The self-organizing map, *Proceedings of the IEEE*, 78, 1464–1480, <https://doi.org/10.1109/5.58325>, 1990.
- Korolev, A. and Isaac, G.: Phase transformation of mixed-phase clouds, *Quarterly Journal of the Royal Meteorological Society*, 129, 19–38,
<https://doi.org/10.1256/qj.01.203>, 2003.
- Korolev, A. and Leisner, T.: Review of experimental studies of secondary ice production, *Atmospheric Chemistry and Physics*, 20, 11 767–
565 11 797, <https://doi.org/10.5194/acp-20-11767-2020>, 2020.
- Korolev, A., McFarquhar, G., Field, P. R., Franklin, C., Lawson, P., Wang, Z., Williams, E., Abel, S. J., Axisa, D., Borrmann, S., Crosier, J.,
Fugal, J., Krämer, M., Lohmann, U., Schlenczek, O., Schnaiter, M., and Wendisch, M.: Mixed-Phase Clouds: Progress and Challenges,
Meteorological Monographs, 58, 5.1–5.50, <https://doi.org/10.1175/AMSMONOGRAPHS-D-17-0001.1>, 2017.
- Lauber, A., Kiselev, A., Pander, T., Handmann, P., and Leisner, T.: Secondary Ice Formation during Freezing of Levitated Droplets, *Journal*
570 *of the Atmospheric Sciences*, 75, 2815–2826, <https://doi.org/10.1175/JAS-D-18-0052.1>, 2018.
- Lin, B., Minnis, P., and Fan, A.: Cloud liquid water path variations with temperature observed during the Surface Heat Budget of the Arctic
Ocean (SHEBA) experiment, *Journal of Geophysical Research: Atmospheres*, 108, <https://doi.org/10.1029/2002JD002851>, 2003.
- Liu, Y., Key, J. R., Vavrus, S., and Woods, C.: Time Evolution of the Cloud Response to Moisture Intrusions into the Arctic during Winter,
Journal of Climate, 31, 9389–9405, <https://doi.org/10.1175/JCLI-D-17-0896.1>, 2018.
- 575 Maksimovich, E. and Vihma, T.: The effect of surface heat fluxes on interannual variability in the spring onset of snow melt in the central
Arctic Ocean, *Journal of Geophysical Research: Oceans*, 117, 2011JC007 220, <https://doi.org/10.1029/2011JC007220>, 2012.
- Matrosov, S. Y.: Retrievals of vertical profiles of ice cloud microphysics from radar and IR measurements using tuned re-
gressions between reflectivity and cloud parameters, *Journal of Geophysical Research: Atmospheres*, 104, 16 741–16 753,
<https://doi.org/10.1029/1999JD900244>, 1999.
- 580 Medeiros, B., Deser, C., Tomas, R. A., and Kay, J. E.: Arctic Inversion Strength in Climate Models, *Journal of Climate*, 24, 4733–4740,
<https://doi.org/10.1175/2011JCLI3968.1>, 2011.



- Mioche, G., Jourdan, O., Ceccaldi, M., and Delanoë, J.: Variability of mixed-phase clouds in the Arctic with a focus on the Svalbard region: a study based on spaceborne active remote sensing, *Atmospheric Chemistry and Physics*, 15, 2445–2461, <https://doi.org/10.5194/acp-15-2445-2015>, 2015.
- 585 Morrison, H., De Boer, G., Feingold, G., Harrington, J., Shupe, M. D., and Sulia, K.: Resilience of persistent Arctic mixed-phase clouds, *Nature Geoscience*; London, 5, 11–17, <https://doi.org/http://dx.doi.org.ezp-prod1.hul.harvard.edu/10.1038/ngeo1332>, 2012.
- Philipp, D., Stengel, M., and Ahrens, B.: Analyzing the Arctic Feedback Mechanism between Sea Ice and Low-Level Clouds Using 34 Years of Satellite Observations, *Journal of Climate*, 33, 7479–7501, <https://doi.org/10.1175/JCLI-D-19-0895.1>, 2020.
- Pithan, F. and Mauritsen, T.: Arctic amplification dominated by temperature feedbacks in contemporary climate models, *Nature Geoscience*, 7, 181–184, <https://doi.org/http://dx.doi.org.ezp-prod1.hul.harvard.edu/10.1038/ngeo2071>, 2014.
- 590 Pithan, F., Svensson, G., Caballero, R., Chechin, D., Cronin, T. W., Ekman, A. M. L., Neggers, R., Shupe, M. D., Solomon, A., Tjernström, M., and Wendisch, M.: Role of air-mass transformations in exchange between the Arctic and mid-latitudes, *Nature Geoscience*, 11, 805–812, <https://doi.org/10.1038/s41561-018-0234-1>, 2018.
- Sedlar, J. and Tjernström, M.: Stratiform Cloud—Inversion Characterization During the Arctic Melt Season, *Boundary-Layer Meteorology*, 132, 455–474, <https://doi.org/10.1007/s10546-009-9407-1>, 2009.
- 595 Shupe, M. D.: Clouds at Arctic Atmospheric Observatories. Part II: Thermodynamic Phase Characteristics, *Journal of Applied Meteorology and Climatology*, 50, 645–661, <https://doi.org/10.1175/2010JAMC2468.1>, 2011.
- Shupe, M. D. and Intrieri, J. M.: Cloud Radiative Forcing of the Arctic Surface: The Influence of Cloud Properties, Surface Albedo, and Solar Zenith Angle, *Journal of Climate*, 17, 616–628, [https://doi.org/10.1175/1520-0442\(2004\)017<0616:CRFOTA>2.0.CO;2](https://doi.org/10.1175/1520-0442(2004)017<0616:CRFOTA>2.0.CO;2), 2004.
- 600 Shupe, M. D., Uttal, T., and Matrosov, S. Y.: Arctic Cloud Microphysics Retrievals from Surface-Based Remote Sensors at SHEBA, *Journal of Applied Meteorology and Climatology*, 44, 1544–1562, <https://doi.org/10.1175/JAM2297.1>, 2005.
- Shupe, M. D., Matrosov, S. Y., and Uttal, T.: Arctic Mixed-Phase Cloud Properties Derived from Surface-Based Sensors at SHEBA, *Journal of the Atmospheric Sciences*, 63, 697–711, <https://doi.org/10.1175/JAS3659.1>, 2006.
- Shupe, M. D., Walden, V. P., Eloranta, E., Uttal, T., Campbell, J. R., Starkweather, S. M., and Shiobara, M.: Clouds at Arctic Atmospheric Observatories. Part I: Occurrence and Macrophysical Properties, *Journal of Applied Meteorology and Climatology*, 50, 626–644, <https://doi.org/10.1175/2010JAMC2467.1>, 2011.
- 605 Shupe, M. D., Persson, P. O. G., Brooks, I. M., Tjernström, M., Sedlar, J., Mauritsen, T., Sjogren, S., and Leck, C.: Cloud and boundary layer interactions over the Arctic sea ice in late summer, *Atmospheric Chemistry and Physics*, 13, 9379–9399, <https://doi.org/10.5194/acp-13-9379-2013>, 2013.
- 610 Shupe, M. D., Persson, P. O. G., Cox, C. J., Gallagher, M. R., Solomon, A., Sledd, A., Blomquist, B., Brooks, I. M., Costa, D., Osborn, J., Perovich, D., Riikimäki, L., and Uttal, T.: Surface energy budget, clouds, and the two states of the central Arctic atmosphere-sea ice system, *Elementa: Science of the Anthropocene*, in press, 2026.
- Silber, I. and Shupe, M. D.: Insights on sources and formation mechanisms of liquid-bearing clouds over MOSAiC examined from a Lagrangian framework, *Elementa: Science of the Anthropocene*, 10, 000071, <https://doi.org/10.1525/elementa.2021.000071>, 2022.
- 615 Silber, I., Fridlind, A. M., Verlinde, J., Russell, L. M., and Ackerman, A. S.: Nonturbulent Liquid-Bearing Polar Clouds: Observed Frequency of Occurrence and Simulated Sensitivity to Gravity Waves, *Geophysical Research Letters*, 47, e2020GL087099, <https://doi.org/10.1029/2020GL087099>, 2020.
- Silber, I., Fridlind, A. M., Verlinde, J., Ackerman, A. S., Cesana, G. V., and Knopf, D. A.: The prevalence of precipitation from polar supercooled clouds, *Atmospheric Chemistry and Physics*, 21, 3949–3971, <https://doi.org/10.5194/acp-21-3949-2021>, 2021.



- 620 Solomon, A., Shupe, M. D., Persson, P. O. G., and Morrison, H.: Moisture and dynamical interactions maintaining decoupled Arctic mixed-phase stratocumulus in the presence of a humidity inversion, *Atmospheric Chemistry and Physics*, 11, 10 127–10 148, <https://doi.org/10.5194/acp-11-10127-2011>, 2011.
- Solomon, A., Shupe, M. D., Svensson, G., Barton, N. P., Batrak, Y., Bazile, E., Day, J. J., Doyle, J. D., Frank, H. P., Keeley, S., Remes, T., and Tolstykh, M.: The winter central Arctic surface energy budget: A model evaluation using observations from the MOSAiC campaign, *Elementa: Science of the Anthropocene*, 11, 00 104, <https://doi.org/10.1525/elementa.2022.00104>, 2023.
- 625 Stramler, K., Genio, A. D. D., and Rossow, W. B.: Synoptically Driven Arctic Winter States, *Journal of Climate*, 24, 1747–1762, <https://doi.org/10.1175/2010JCLI3817.1>, 2011.
- Toto, T. and Giangrande, S.: Cloud Radar (KAZR, KAZR2, or MWACR) Corrected VAP (KAZRCFRCORGE), 2019-10-28 to 2023-12-31, North Slope Alaska (NSA), Central Facility, Barrow AK (C1), <https://doi.org/10.5439/1560129>, accessed: 2025-01-30, 2019.
- 630 Turner, D. D., Clough, S. A., Liljegren, J. C., Clothiaux, E. E., Cady-Pereira, K. E., and Gaustad, K. L.: Retrieving Liquid Water Path and Precipitable Water Vapor From the Atmospheric Radiation Measurement (ARM) Microwave Radiometers, *IEEE Transactions on Geoscience and Remote Sensing*, 45, 3680–3690, <https://doi.org/10.1109/TGRS.2007.903703>, 2007.
- Verlinde, J., Harrington, J. Y., McFarquhar, G. M., Yannuzzi, V. T., Avramov, A., Greenberg, S., Johnson, N., Zhang, G., Poellot, M. R., Mather, J. H., Turner, D. D., Eloranta, E. W., Zak, B. D., Prenni, A. J., Daniel, J. S., Kok, G. L., Tobin, D. C., Holz, R., Sassen, K., Spangenberg, D., Minnis, P., Tooman, T. P., Ivey, M. D., Richardson, S. J., Bahrman, C. P., Shupe, M., DeMott, P. J., Heymsfield, A. J., and Schofield, R.: The Mixed-Phase Arctic Cloud Experiment, *Bulletin of the American Meteorological Society*, 88, 205–222, <https://doi.org/10.1175/BAMS-88-2-205>, 2007.
- 635 Verlinde, J., Zak, B. D., Shupe, M. D., Ivey, M. D., and Stamnes, K.: The ARM North Slope of Alaska (NSA) Sites, *Meteorological Monographs*, 57, 8.1–8.13, <https://doi.org/10.1175/AMSMONOGRAPHIS-D-15-0023.1>, 2016.
- 640 Walsh, J. E. and Chapman, W. L.: Arctic Cloud–Radiation–Temperature Associations in Observational Data and Atmospheric Reanalyses, *Journal of Climate*, 11, 3030–3045, [https://doi.org/10.1175/1520-0442\(1998\)011<3030:ACRTAI>2.0.CO;2](https://doi.org/10.1175/1520-0442(1998)011<3030:ACRTAI>2.0.CO;2), 1998.
- Wedum, A. E., Pettersen, C., Guy, H., Gallagher, M. R., Shupe, M. D., and Mattingly, K. S.: Impacts of Atmospheric Rivers in Central Greenland: Snowfall, Clouds, and Atmospheric State, *Journal of Geophysical Research: Atmospheres*, 131, e2025JD044 309, <https://doi.org/10.1029/2025JD044309>, 2026.
- 645 Wegener, A.: *Thermodynamik der atmosphäre*, JA Barth, 1911.
- Westwater, E. R., Han, Y., Shupe, M. D., and Matrosov, S. Y.: Analysis of integrated cloud liquid and precipitable water vapor retrievals from microwave radiometers during the Surface Heat Budget of the Arctic Ocean project, *Journal of Geophysical Research: Atmospheres*, 106, 32 019–32 030, <https://doi.org/10.1029/2000JD000055>, 2001.
- Wex, H., Huang, L., Zhang, W., Hung, H., Traversi, R., Becagli, S., Sheesley, R. J., Moffett, C. E., Barrett, T. E., Bossi, R., Skov, H., Hünerbein, A., Lubitz, J., Löffler, M., Linke, O., Hartmann, M., Herenz, P., and Stratmann, F.: Annual variability of ice-nucleating particle concentrations at different Arctic locations, *Atmospheric Chemistry and Physics*, 19, 5293–5311, <https://doi.org/10.5194/acp-19-5293-2019>, 2019.
- 650 Woods, C. and Caballero, R.: The Role of Moist Intrusions in Winter Arctic Warming and Sea Ice Decline, *Journal of Climate*, 29, 4473–4485, <https://doi.org/http://dx.doi.org.ezp-prod1.hul.harvard.edu/10.1175/JCLI-D-15-0773.1>, 2016.
- 655 Woods, C., Caballero, R., and Svensson, G.: Large-scale circulation associated with moisture intrusions into the Arctic during winter, *Geophysical Research Letters*, 40, 4717–4721, <https://doi.org/10.1002/grl.50912>, 2013.



- You, C., Tjernström, M., and Devasthale, A.: Warm and moist air intrusions into the winter Arctic: a Lagrangian view on the near-surface energy budgets, *Atmospheric Chemistry and Physics*, 22, 8037–8057, <https://doi.org/10.5194/acp-22-8037-2022>, 2022.
- Zhang, D.: MWR Retrievals (MWRRET1LILJCLOU), 2001-04-01 to 2023-12-31, North Slope Alaska (NSA), Central Facility, Barrow AK
660 (C1), <https://doi.org/10.5439/1027369>, accessed: 2024-11-04, 2001.
- Zhang, D., Ermold, B., and Morris, V.: Ceilometer (CEIL), 2000-01-01 to 2023-12-31, North Slope Alaska (NSA), Central Facility, Barrow AK (C1), <https://doi.org/10.5439/1181954>, accessed: 2024-10-09, 1997.
- Zhang, T., Stamnes, K., and Bowling, S. A.: Impact of Clouds on Surface Radiative Fluxes and Snowmelt in the Arctic and Subarctic, *Journal of Climate*, 9, 2110–2123, [https://doi.org/10.1175/1520-0442\(1996\)009<2110:IOCOSR>2.0.CO;2](https://doi.org/10.1175/1520-0442(1996)009<2110:IOCOSR>2.0.CO;2), 1996.
- 665 Zhang, X., Schneider, T., and Kaul, C. M.: Sensitivity of idealized mixed-phase stratocumulus to climate perturbations, *Quarterly Journal of the Royal Meteorological Society*, 146, 3285–3305, <https://doi.org/10.1002/qj.3846>, 2020.
- Zuidema, P., Baker, B., Han, Y., Intrieri, J., Key, J., Lawson, P., Matrosov, S., Shupe, M., Stone, R., and Uttal, T.: An Arctic Springtime Mixed-Phase Cloudy Boundary Layer Observed during SHEBA, *Journal of the Atmospheric Sciences*, 62, 160–176, <https://doi.org/10.1175/JAS-3368.1>, 2005.